SCIENTIFIC-SPECIALIZED JOURNAL
# NEW RESEARCH ON ENGINEERING SCIENCES

Scientific-Specialized Journal Of New Research On Engineering Sciences
No 17, May 2018



NRES.ir

SCIENTIFIC-SPECIALIZED JOURNAL

# NEW RESEARCH ON ENGINEERING SCIENCES

Journal Of New Research On Engineering Sciences
Volume 3, Issue 2(17), May 2018

# پژوهش های نوین علوم مهندسی

ماهنامه علمی-تخصصی پژوهش‌های نوین علوم مهندسی،
سال سوم، شماره هفده ، خردادماه ۱۳۹۷



۰۲۱ ۴۳ ۸۵ ۷۱ ۲۴
۰۲۶ ۳۲ ۷۴ ۷۱ ۵۸
۰۲۱ ۳۳ ۲۰ ۲۴ ۸۷
۰۲۶ ۳۲ ۷۲ ۴۷ ۸۷
تهران: افسریه،۱۵متری چهارم،کوچه ۳۸، پلاک ۲۸، واحد۲
کرج: چهارراه هفت‌تیر،خیابان لاله ۱،پلاک ۱۴،طبقه‌همکف

# Content

# Jet Trajectory in Tangentially-fired Single Chamber Furnaces with Square Horizontal Cross-sections

**Amin Lotfiani**
*Assistant Professor, Mechanical Engineering Department, Elm-o-Fann University College of Science and Technology, Urmia, Iran*
*Email: amn622002@gmail.com*

## Abstract

In this work, jet trajectory in the flow field of tangentially-fired furnaces (TFF) with square horizontal cross-sections is studied using three-dimensional computational fluid dynamics (CFD) simulations. A least-squares correlation for the trajectory of the coaxial fuel-air jets is suggested which can be very useful in future analysis of TFF. In order to verify the CFD solution procedure, a turbulent round jet injected into cross-flow is simulated. The calculated jet trajectory and velocity profile are compared with the experimental and numerical data of existing references and good agreement is observed. Results show that the trajectory of the coaxial fuel-air jets is neither affected by the inner (fuel) jet Reynolds number nor by the outer-to-inner jet momentum ratio.

**Keywords**: Jet trajectory, tangentially-fired furnace, diffusion combustion, CFD

## 1. Introduction

In most industrial combustion and flame applications, the achievement of high heat transfer rates and low pollutant emissions using diffusion furnaces is a target and is desirable. Uniform heat flux in industrial furnaces is of great importance because local overheating and high thermal stresses result in components failure and shorter furnace lifetime. Taking account of different parameters, engineers have continuously modified furnaces to meet the above-mentioned requirements. Tangentially-fired furnaces (TFF) are one of the modified types of furnaces which have become more attractive in the field of industrial firing systems in the last years. They have been used extensively throughout the world with wide applications in power station boilers. In these furnaces, several coaxial fuel-air jets are directed at an imaginary circle in the middle of the furnace to bring about a vortex motion. Each coaxial jet impinges upon the adjacent jet and deflects it. Thus the initially-free coaxial fuel-air jets no longer remain free after the impingement. Operating characteristics, flow pattern, mixing, heat transfer, and combustion in these furnaces have not yet been adequately studied. Some recent works on TFF are introduced below.

Vagner (2004) experimentally studied a tangentially coal-fired cogeneration plant boiler in order to raise its thermal efficiency and to reduce the harmful emissions. The boiler was reconstructed and stage firing of coal in a U-shaped flame was organized. Habib *et al* (2005) numerically studied the flow field and thermal characteristics in a model of a TFF under different conditions of burner tripping. They showed that tripping one or two burners either adjacent or opposite results in high temperature regions close to the walls. Belosevic *et al* (2006) presented numerical simulations of processes in a tangentially-fired utility boiler furnace burning coal. Their three-dimensional simulations were based on a specially-developed comprehensive mathematical model. Different grinding fineness of coal and coal quality were investigated. They also performed measurements to validate their numerical results. Diez *et al* (2008) numerically investigated $NO_x$ emissions from a tangentially-fired utility boiler under conventional and overfire air operating conditions. They validated the results of their computational fluid dynamics (CFD) simulation against actual measurements and demonstrated the feasibility and strength of this type of analysis tool. Li *et al* (2009) performed full-scale experiments on a 300 MWe tangentially-fired utility boiler retrofitted with air staging. They investigated the influencing factors including the overall excessive air ratio, the secondary air distribution pattern, the damper openings of separated overfire air (SOFA) and close coupled overfire air (CCOFA), and pulverized coal fineness to improve the boiler thermal efficiency and to reduce $NO_x$ emission. Zhou *et al* (2009) studied the flow field in upper furnace of large scale tangentially-fired boilers numerically and experimentally. They clearly showed the forming mechanism of flue gas velocity and temperature deviation and the effect of furnace arch and platen superheaters on residual air flow swirl and gas velocity deviation in large scale tangentially-fired boilers. Modlinski (2010) numerically investigated a utility boiler TFF using three-dimensional CFD simulations. The traditional jet burners were replaced with rapid ignition swirl burners to enhance the combustion of pulverized coal and the furnace performance.

In the present work, three-dimensional CFD simulations are employed to study the trajectory of coaxial fuel-air jets in the flow field of a TFF with square horizontal cross-sections. The same definition of jet trajectory is used as was used by Kamotani and Greber (1972). Jet trajectory is the locus of the maximum velocity in the plane of symmetry. A least-squares correlation for the trajectory of the coaxial jets is suggested. In order to verify the CFD solution procedure, a turbulent round jet injected into cross-flow is simulated. The calculated jet trajectory and velocity profile are compared with the experimental and numerical data of existing references and good agreement is observed. Results can be very useful in future analysis of TFF.

## 2. Problem specifications

### 2.1 Details of the furnace

In the TFF of the present study, four coaxial fuel-air jets are admitted into the combustion chamber in a tangential manner from its sides. Fuel enters the combustion chamber from a round nozzle of diameter 10 mm and air is admitted through an annulus surrounding the central fuel nozzle. The larger diameter of the annular air passage is 30 mm. The coaxial fuel-air jets are directed at an imaginary circle 50 mm in diameter in the middle of the furnace. The opposite burners are the same distance (50 mm) apart laterally. Each coaxial jet impinges upon the adjacent jet and deflects it. Thus the initially-free coaxial fuel-air jets no longer remain free after the impingement. The side length of the furnace square cross-section is 560 mm. Part of the above-mentioned furnace is simulated to study the jet trajectory, under isothermal conditions. This part is 150 mm high and the burners are accommodated midway between its top and bottom faces. Operating pressure is 101325 Pa and the flow is assumed to be at a constant temperature of 300 K. Geometry and dimensions of the furnace and details of the coaxial nozzles are shown in Figure 1.

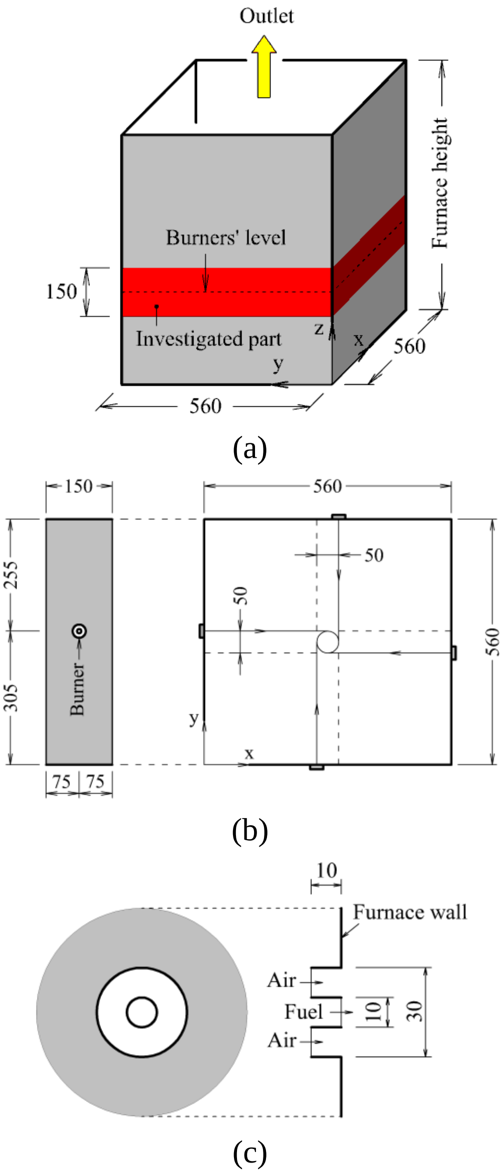


**Figure 1: a) Geometry and dimensions (in mm) of the furnace chamber; b) Arrangement of the burners; c) Details of the coaxial nozzles**

### 2.2 Influencing parameters

With the assumption that the trajectory of a round fuel jet in the flow field of TFF is only a function of the jet fluid density $\rho_f$ and viscosity $\mu_f$, velocity at the nozzle exit $v_f$, nozzle diameter $d_1$, and the side length of the furnace square cross-section $L$, dimensional analysis yields:

$$\frac{x}{L} = f_1\left(\frac{y}{L}, \frac{\rho_f v_f d_1}{\mu_f}\right) = f_1\left(\frac{y}{L}, \text{Re}\right) \qquad (1)$$

Taking account of the air jet which is admitted into the combustion chamber through the annular passage around the central fuel nozzle, additional parameters such as air density $\rho_a$, velocity at the exit of the annular air nozzle $v_a$, the larger diameter of the annular air nozzle $d_2$, and the dynamic viscosity of air $\mu_a$ must be included in the analysis. In this case, dimensionless groups MR and $\mu_a/\mu_f$ are added to those in Equation (1). MR is the momentum ratio, i.e. the ratio of the outer (air) jet momentum to the inner (fuel) jet momentum (Lotfiani *et al*, 2013). Since high Reynolds numbers are used in most of the practical combustion systems, the ratio of inertial forces to viscous forces is high and it is reasonable to neglect the effect of $\mu_a/\mu_f$ on the jet trajectory compared to the other dimensionless groups. Therefore,

$$\frac{x}{L} = f_2(\frac{y}{L}, \mathrm{Re}, \mathrm{MR}) \qquad (2)$$

In subsequent sections, three-dimensional CFD simulations will be carried out to study the effect of Re and MR on the trajectory of the coaxial fuel-air jets in the flow field of TFF.

## 3. Modeling and computations

The mathematical model is based on the solution of the continuity, momentum and turbulence model equations for incompressible flow. The assumption of incompressibility is valid since all the simulations are carried out at subsonic speeds with the largest Mach number being approximately 0.3. Eddy viscosity is determined using the two-equation Realizable $k$-$\varepsilon$ turbulence model because this model addresses the deficiencies of the traditional $k$-$\varepsilon$ models (Fluent 6.2 user's guide, 2005; Habib *et al*, 2005; Lotfiani *et al*, 2009; Modlinski, 2010). Since the governing equations can easily be found in many references (e.g. see Fluent 6.2 user's guide, 2005; Habib *et al*, 2005; Lotfiani, 2012; Zhou *et al*, 2009), they are not repeated here.

The calculations are performed under isothermal conditions using the flow solver Fluent 6.2. In the simulations, air is used as the inner (fuel) jet fluid for simplicity. All the governing equations are discretized using the second-order upwind scheme. The discretized equations are solved using the Simple algorithm. The implicit and segregated solver is applied for the solution of the system of governing equations. The software Gambit 2.2 is employed to generate the geometry and mesh for the computational domain. Computations are performed on three progressively finer meshes to secure grid independence. Results are virtually identical for the three meshes and the minor grid dependence of the results is safely neglected. The chosen mesh consists of 59833 high quality cells. Most of the cells are hexahedral and a few are tetrahedral/hybrid. To capture the details of the flow accurately, the size of the cells is significantly reduced near the nozzles and the furnace center where large gradients are expected. This three-dimensional mesh is demonstrated in Figure 2.

As indicated in Figure 2, only one quarter of the whole geometry is meshed. This is made possible through the use of the periodic boundary condition, since the geometry and expected flow pattern are rotationally repetitive in nature. This helps reduce the computational effort, without compromising the accuracy. Velocity inlet boundaries are used at the fuel and air inlets and pressure outlet boundary is used at the top and bottom faces of the investigated part. Wall boundary with constant temperature of 300 K and no slip condition is used at the chamber walls. Turbulence intensity is assumed to be 5% at the fuel and air inlets and also at the top and bottom faces of the investigated part. Convergence criterion for all the governing equations is the residual value. Solution is considered to be converged when the residual values become less than $10^{-5}$. It takes about 2 hours for each solution to converge.

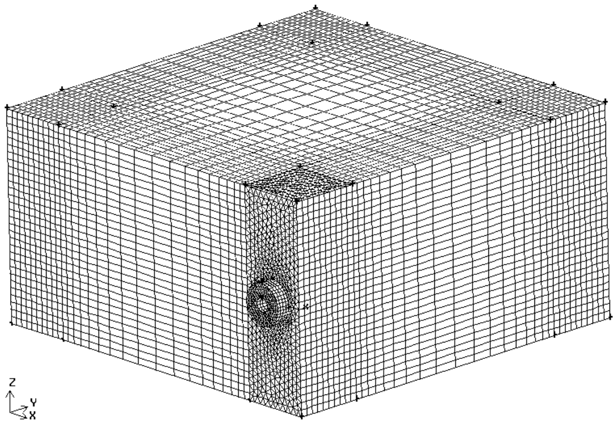


**Figure 2: The high quality three-dimensional mesh consisting of 59833 cells**

## 4. Results and discussion

There is still a lack of usable measurements of flow field in TFF. Hence a turbulent round jet injected into cross-flow is simulated to verify the CFD solutions of the present work because it is a characteristic feature of the flow in TFF. The calculated jet trajectory is compared with the experimental data of Kamotani and Greber (1972). The experimental data of Crabb *et al* (1981) and the large eddy simulation (LES) of Majander and Siikonen (2006) are used to evaluate the velocity profile. Figure 3-a shows the trajectory of the turbulent round jet in cross-flow. The origin of coordinates is placed at the center of the nozzle exit. The $x$ axis is taken in the cross-flow direction and the $z$ axis is the centerline of the round nozzle. The ratio of the jet momentum to that of the cross-flow is $J$=32 and $y$=0 denotes the symmetry plane of the deflected jet. The jet and the cross-flow fluid is air. The $x$-velocity distribution at $y$=0 and $x/D$=6 is shown in Figure 3-b. Here, $D$ is the round nozzle diameter, $U$ is the $x$ velocity component, and $U_{cf}$ is the uniform cross-flow velocity. It can be seen that the present CFD simulations compare favorably with the available experimental and numerical data.

Samples of the flow pattern in TFF with square horizontal cross-sections are shown in Figure 4. Contours of velocity magnitude (in m/s) at the burners' level corresponding to the TFF of the present study with Re=32888 and MR=1.5 are shown in Figure 4-a. In addition, the flow pattern in two previously-simulated TFF burning methane is indicated in Figures 4-b and 4-c. More details about these two furnaces are given in the previous works of the author (Khalilarya and Lotfiani, 2010; Lotfiani *et al*, 2012).

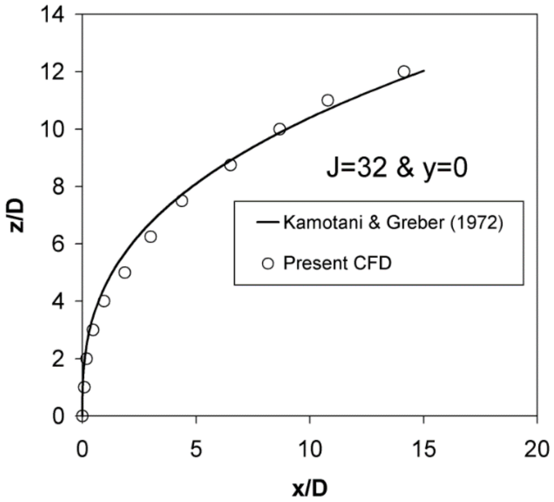


(a)

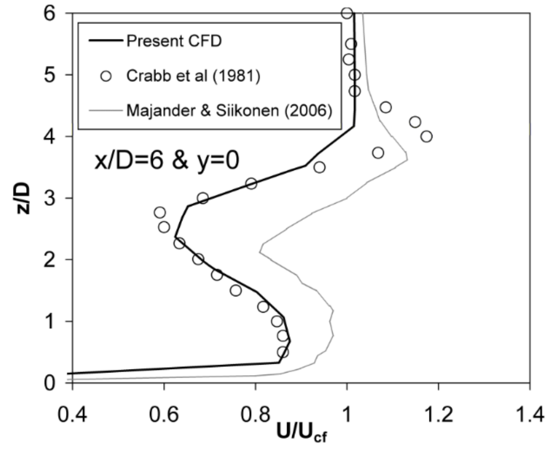


(b)

**Figure 3: Validation of the present CFD simulations: a) The trajectory of the turbulent round jet in cross-flow; b) Distribution of the *x*-velocity at *y*=0 and *x*/*D*=6**

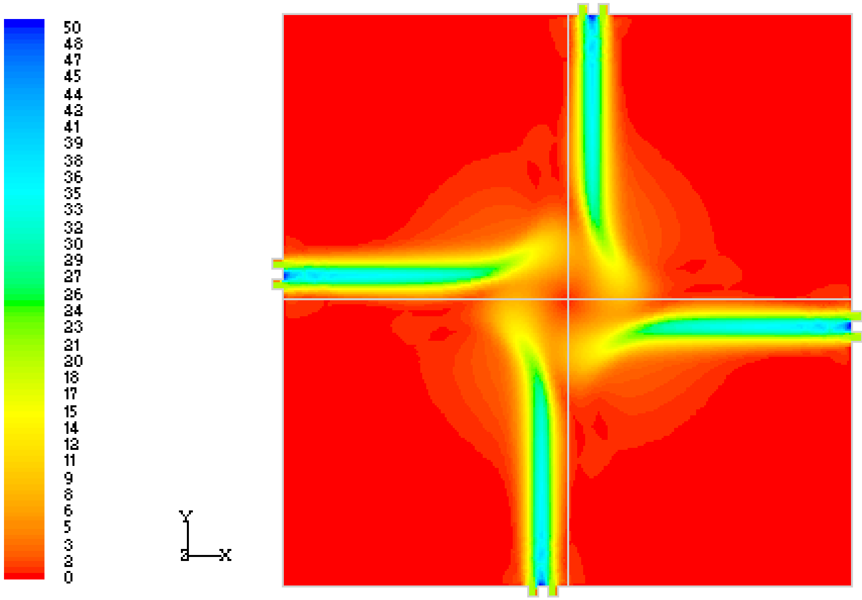
50
48
47
45
44
42
41
39
38
36
35
33
32
30
29
27
26
24
23
21
20
18
17
15
14
12
11
9
8
6
5
3
2
0
Y
X

(a)

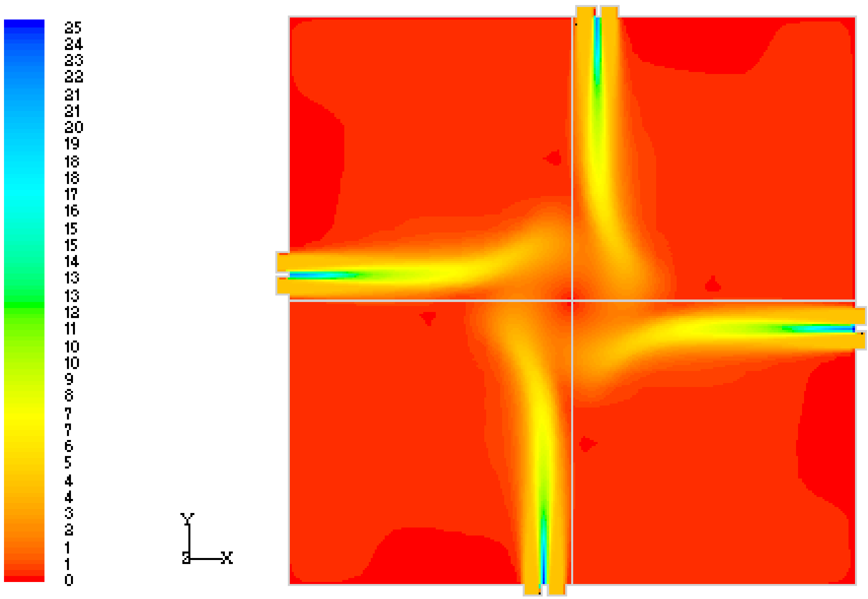
25
24
23
22
21
21
20
19
18
18
17
16
15
15
14
13
13
12
11
10
10
9
8
7
7
6
5
4
4
3
2
1
1
0
Y
X

(b)

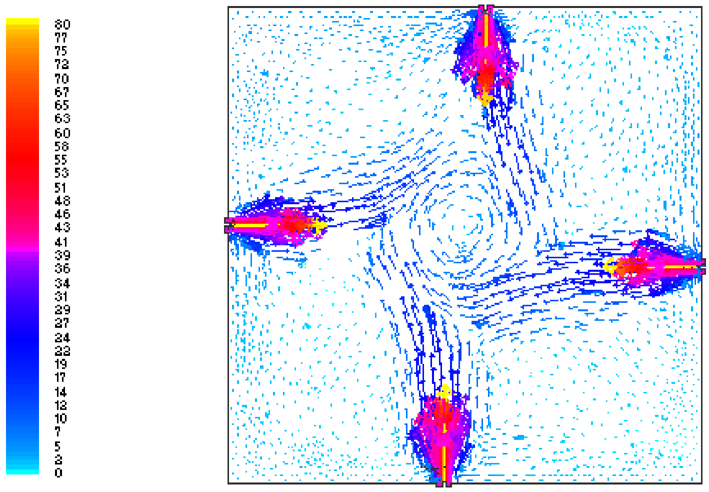


(c)

**Figure 4: Samples of the flow pattern in TFF at the burners' level: a) Contours of velocity magnitude (in m/s) in the TFF of the present study; b) Contours of velocity magnitude (in m/s) in the TFF previously studied by Lotfiani *et al* (2012); c) Velocity vectors in the TFF previously studied by Khalilarya and Lotfiani (2010)**

It can be seen that each of the four coaxial jets impinges upon the adjacent jet and deflects it. This creates a vortex in the middle of the furnace. The vortex entrains lean and rich zones and blends them together. This ensures an efficient mixing of fuel with air and, in turn, a reliable combustion with uniform temperature distribution (Habib *et al*, 2005; Khalilarya and Lotfiani, 2010; Lotfiani, 2012; Lotfiani *et al*, 2012). Velocity vectors in Figure 4-c clearly show the deflection of the coaxial jets and the vortex created in the middle of the furnace.

Figure 5 demonstrates how Re and MR affect the trajectory of the coaxial fuel-air jets in the flow field of TFF with square horizontal cross-sections. The jet trajectory at different Reynolds numbers and different momentum ratios is shown in Figures 5-a and 5-b, respectively. The study is carried out only in one quarter of the furnace because of the rotationally-repetitive flow pattern in TFF. It can be observed that neither of the above-mentioned parameters has influence on the jet trajectory.

As shown in Figure 5, the jet remains intact and straight up to $y/L$=0.321. Then it deflects up to $y/L$=0.464 and finally continues its way in a straight line parallel to the symmetry axis of the coaxial nozzles up to $y/L$=0.500.

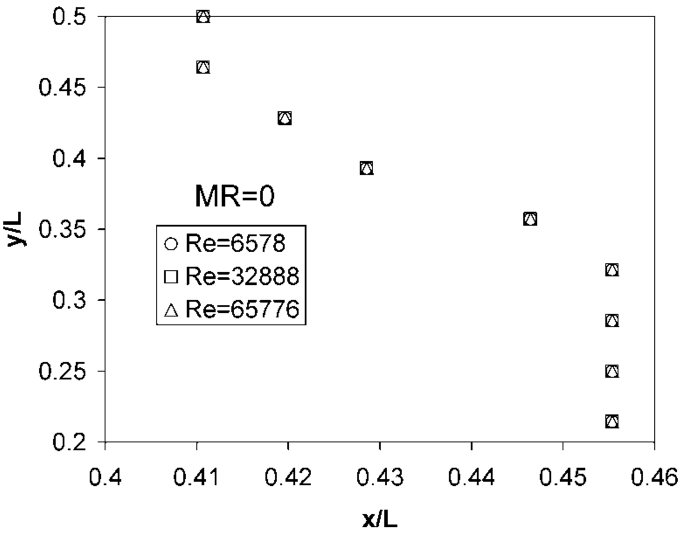


(a)

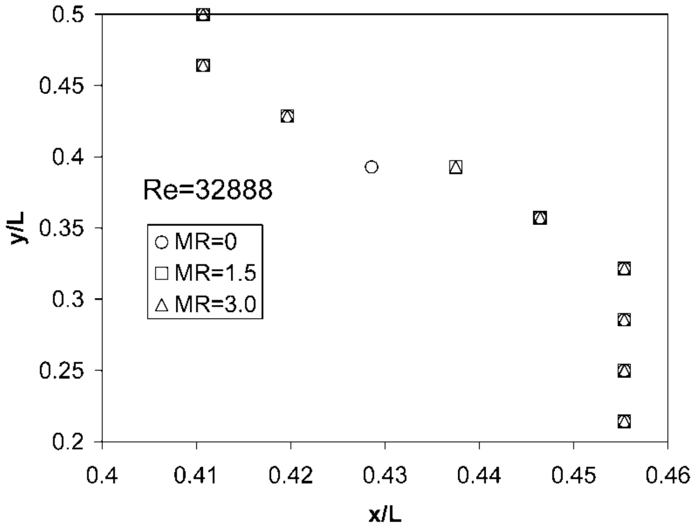


(b)

**Figure 5: The trajectory of the coaxial fuel-air jets in the flow field of TFF, a) at different Reynolds numbers; b) at different momentum ratios**

The trajectory of the jet flowing in the positive direction of the y axis can be approximated by a third-order polynomial in the interval 0.321<y/L<0.464 as follows:

$$\frac{1}{L}\left(x-\frac{1}{2}(L-d_{\text{imag}})\right)=c_3'\left(\frac{y}{L}\right)^3+c_2'\left(\frac{y}{L}\right)^2+c_1'\left(\frac{y}{L}\right)+c_0' \qquad (3)$$

where

$$c_0'=-1.6959,\ c_1'=13.7179,\ c_2'=-36.1122,\ c_3'=30.6407$$

This is shown in Figure 6. As suggested by Romadin (1974), the imaginary circle diameter (see Figure 1-b) $d_{\text{imag}}$ in Equation (3) is adjusted to be 0.089$L$.

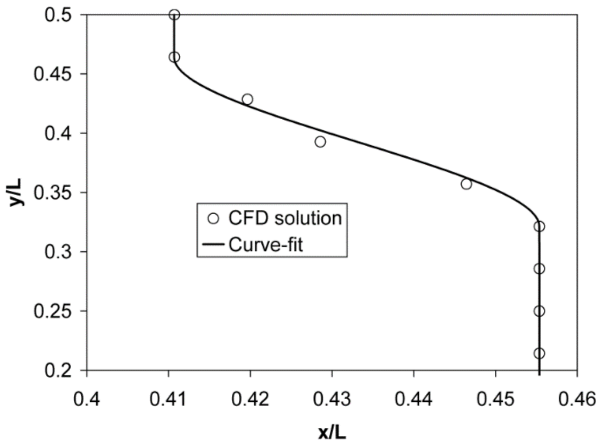


**Figure 6: Least-squares correlation for the trajectory of the coaxial fuel-air jets**

## 5. Conclusions

In the present study, the trajectory of coaxial fuel-air jets in the flow field of TFF with square horizontal cross-sections is investigated by making three-dimensional CFD simulations. The simulations are made under isothermal conditions using the flow solver Fluent 6.2. In order to verify the CFD solution procedure, a turbulent round jet injected into cross-flow is simulated. The calculated jet trajectory and velocity profile are compared with the experimental and numerical data of existing references and good agreement is observed. Results show that the trajectory of the coaxial fuel-air jets is neither affected by the inner (fuel) jet Reynolds number nor by the outer-to-inner jet momentum ratio. According to the results, a third-order polynomial can predict the trajectory of the deflected coaxial jets very well.

## References


- Belosevic, S. *et al*. (2006) Three-dimensional modeling of utility boiler pulverized coal tangentially fired furnace, *International Journal of Heat and Mass Transfer*, 49, pp. 3371-3378.
- Crabb, D. *et al*. (1981) A round jet normal to a crossflow, *Journal of Fluids Engineering*, 103, pp. 568-580.
- Diez, L.I. *et al*. (2008) Numerical investigation of $NO_x$ emissions from a tangentially-fired utility boiler under conventional and overfire air operation, *Fuel*, 87, pp. 1259-1269.
- Fluent Inc. (2005) *Fluent 6.2 user's guide*. Lebanon: NH 03766, USA.
- Habib, M.A. *et al*. (2005) Flow field and thermal characteristics in a model of a tangentially fired furnace under different conditions of burner tripping, *Heat Mass Transfer*, 41, pp. 909-920.
- Kamotani, Y. and Greber, I. (1972) Experiments on a turbulent jet in a cross flow, *AIAA Journal*, 10, pp. 1425-1429.
- Khalilarya, Sh. and Lotfiani, A. (2010) Determination of flow pattern and its effect on $NO_x$ emission in a tangentially fired single chamber square furnace, *Thermal Science*, 14 (2), pp. 493-503.
- Li, S. *et al*. (2009) $NO_x$ emission and thermal efficiency of a 300 MWe utility boiler retrofitted by air staging, *Applied Energy*, 86, pp. 1797-1803.
- Lotfiani, A. (2012) *A multi-zone model for the simulation of tangentially gas-fired furnaces with square horizontal cross-section*. Ph.D Thesis, Urmia University, Urmia, Iran.
- Lotfiani, A. *et al*. (2009) Evaluation of two-equation turbulence models for the simulation of gaseous round jets (in Farsi), in: *Proceedings of 2009 Mechanical Engineering Conference*, Mashhad, Iran, November 2009. pp. 210-211.

- Lotfiani, A. *et al*. (2012) Comparison of flow and mixing in a gas-fired furnace in tangential and opposed injection modes. in: *Proceedings* of the 20th Annual International Conference on Mechanical Engineering-ISME2012, Shiraz, Iran, May 2012. pp. 46-49.
- Lotfiani, A. *et al*. (2013) A semi-analytical model for the prediction of the behavior of turbulent coaxial gaseous jets, *Thermal Science*, 17 (4), pp. 1221-1232.
- Majander, P. and Siikonen, T. (2006) Large-eddy simulation of a round jet in a cross-flow, *International Journal of Heat and Fluid Flow*, 27, pp. 402-415.
- Modlinski, N. (2010) Computational modeling of a utility boiler tangentially-fired furnace retrofitted with swirl burners, *Fuel Processing Technology*, 91, pp. 1601-1608.
- Romadin, V.P. (1974) Furnaces with corner firing tangential burners, *Thermal Engineering*, 20, pp. 79-89.
- Vagner, A.A. (2004) Raising the reliability, efficiency, and ecological safety of operation of the BKZ-210-140F boiler transferred to stage firing of Kuznetsk coal in a U-shape flame, *Power Technology and Engineering*, 38 (3), pp. 159-163.
- Zhou, Y. *et al*. (2009) Experimental and numerical study on the flow field in upper furnace for large scale tangentially fired boilers, *Applied Thermal Engineering*, 29, pp. 732-739.

# Comparing the Efficiency of Seismic Isolation and Seesaw Motion in Multi-story Regular Steel Buildings for Achieving the Immediate Occupancy Performance Level

**Soroush Kherad*[1], Mahmood Hosseini[2]**
1- Doctorate Student, Islamic Azad Univ., Tehran South Branch
*(Email: soroushkherad@gmail.com)*
2- Associate Prof., Int'l Inst. of Earthquake Eng. & Seismology (IIEES)

**ABSTRACT**
There are some important buildings which their performance level (PL) should not be lower than immediate occupancy (IO) based on the recent seismic design codes. The most common way for achieving this PL is using seismic isolation technique. However this technique has not been acknowledged worldwide so much, particularly in developing countries, mainly due to the high cost and the relatively large required free space around the building which is not usually acceptable for the buildings' owners. Another approach for achieving IO PL, proposed in recent years, is using a structural system which can have seesaw motion during an earthquake, and at the same time dissipate a major part of the input energy in its specific dampers or structural fuses, which can be easily replaced after the earthquake. The building with such a system which can be called 'seesaw building' needs to have, in addition to the structural fuses, a specific central support and a grid of strong girders at its lowest floor. These additional components add some cost to the costs of the building's structural system. The aim of this study is comparing the efficiency of common seismic isolation technique with that of the seesaw building, from both seismic performance and construction costs aspects. Special attention has been paid to the near-field earthquake to which the common isolation systems are weak. For comparing the seismic behaviors of the two systems, responses of the considered counterpart buildings have been obtained by a series of nonlinear time history analysis by using a set of selected far- and near-field earthquakes. Numerical results show that the seesaw building generally behaves better than isolated buildings, with less lateral displacements, and its cost is relatively lower as well. The only shortcoming of the seesaw building is its very little residual displacement at the end of the earthquake, which necessitates some attempts for bringing it back to the original position.

**KEYWORDS:** Repairable building, Structural fuse, nonlinear time history analysis, Near-field earthquake

## 1- Introduction

In structural engineering, the mitigation of damage induced by large loads is of paramount interest. Especially in seismic regions, earthquakes pose a serious threat to human lives and the integrity of the infrastructure. Passive energy dissipating systems such as viscous dampers, tuned mass dampers and base isolation systems have been installed in new or existing buildings (Noroozinejad and Adnan 2012, Matta 2011, Konara and Ghosh 2010, Fujita et al. 2010a,b, Patel and Jangid 2011, Silvestri et al. 2011, Abbas and Kelly 1993, Ahlawat and Ramaswamy 2000, Aiken et al. 1990, Ashour and Hanson 1987, Bhaskararao and Jangid 2006, Chang et al.

1993, Cherry and Filiatrault 1993, Kasai et al. 1998, Pong et al. 1994, Shen and Soong 1995, Boller et al. 2009, Singh and Moreschi 2000, Soong and Dargush 1997, Zhang and Soong 1992). Base isolation is one of the most widely used and accepted seismic protection systems.

The philosophy behind most of seismic design codes implicitly accepts heavy damages of the building in case of large earthquakes, provided that the building is prevented against collapse. However, this philosophy, in case of large populated cities located in the vicinity of active faults, leads to unacceptable consequences, such as large number of people who lose their living or working places for a long time, very difficult demolishing work of the heavily damaged buildings, and very large volume of the required reconstruction works. To avoid these adverse consequences one approach is design of 'repairable structures' for buildings, by using the idea of 'Deliberate Directing of Damage' (DDD), introduced by the first author (Hosseini and Alyasin 1996), which means guiding the damage to some pre-decided parts or elements of the structural system, so that other parts do not experience any plastic deformation, and therefore, the structure can be easily repaired. Although this technique has been introduced basically for pipelines, researchers have introduced and worked on similar ideas for other types of structures, particularly building systems, among them using the energy dissipating devices or structural fuses can be mentioned, which have been introduced in late 70s to early 80s (Fintel and Ghosh 1981), and have been developed more in recent years (Vargas and Bruneau 2006). It should be noted that in these studies, although the main idea is concentration of damage in energy dissipaters or fuses, and keeping the main structural members elastic or with minor easily repairable damages, in reality the building cannot remain in Immediate Occupancy (IO) Performance Level (PL), and needs to be evacuated, at least partially, for repair works. To overcome this shortcoming, the use of rocking motion of the building has been proposed by some researchers in recent decade (Midorikawa et al. 2002). They used weak base plates, attached to the bottom of each steel column at the first story, to cause rocking vibration under appropriate control, and conducted more recently an experimental study on a structural frame with rocking motion (Azuhata et al. 2008). Although their proposed rocking structural system is quite effective is seismic response reduction, their studies is limited to 2-dimensional systems. Recently, the first author of this paper has used the idea of rocking motion of building in combination with a central fuse, which works as a huge plastic hinge under the vertical load and the moment, induced by the lateral seismic load (Hosseini and Kherad 2013). In this study the DDD idea has been employed for design of regular steel multi-storey buildings, which have rocking motion, by using inclined columns around the central main vertical column of the building at its base level. The inclined columns, which their bases have been shifted toward the centre of the building plan and cause the building to move basically in rocking motion during an earthquake, are equipped with Double-ADAS (DADAS) devices (Hosseini and Bozorgzadeh 2013), which play the main role of energy dissipating devices or fuses. The inclined columns are connected to the strong beams of the first floor of the building, whose strength and relatively high stiffness help the upper floors of the building to remain elastic, while the DADAS devices experience large 3 plastic deformations and absorb large amounts of seismic input energy. At corners of the building at the base level some cables with initial slackness are used to make the building secure against overturning in case of excessive rocking motion. In this way, the building will have more reliably the IO PL after major earthquakes. The efficiency of the proposed technique has been shown through implementation in some high-rise hybrid steel buildings. Details of the study are given in the following sections.

## 2- The Proposed Rocking Structural System

### 2-1- Tables and Figures of damper

In the proposed rocking structural system for regular multi-storey steel buildings, creation of possibility of rocking motion has been done by using a space truss resting on a huge central hinge support at base level with a series of circumferential energy dissipating mini columns at that base level. Energy dissipation in each of these columns is done by using a multiple curved Yielding-Plate Energy Dissipating device that called cat eye shape damper (CED), which is installed at the bottom of the column as shown in Figure 1.

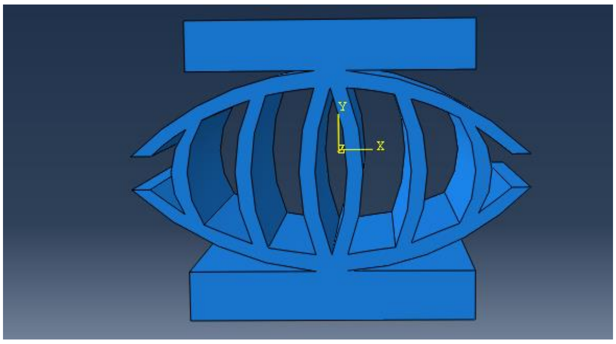


**Fig. 1: The CED device used at the bottom of the circumferential Columns at the rocking building's base level.**

As shown in Figure 1, each CED device consists of multi curve plate in the canter of fuse and two curved plate in the around that connect in up and down by two rigid plate that the force of columns is take here, and a set of curved plates which is connected to the outer plate and their out sides fixed by rigid plate that set in button of column. During an earthquake the vertical movement of the column, which is in fact the lower part of the column element, cause the week and curved plates to yield. Curved form of the yielding plates causes the plastic deformation to develop in the majority of their body, leading to remarkable energy dissipation and creating a type of hysteretic behaviour in axial deformation of columns, as shown in Figure 2, which shows a section of the deformed shape of the CED device, and a sample of its hysteretic curves.

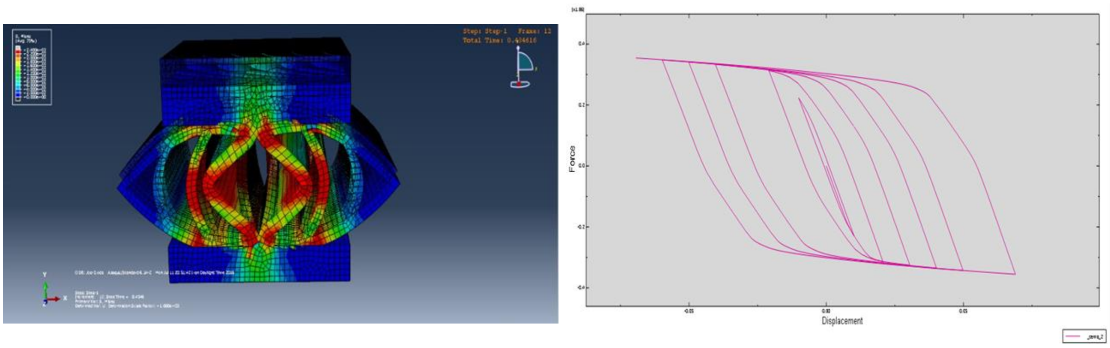


**Fig. 2: A section of the deformed shape of the CED device (upper) And a sample of its hysteretic curves (lower)**

In Figure 3 the circumferential columns of the base level are shown as multi-linear links with hinge connection at their both ends. It is seen in Figure 3 that the building structure above the lowest level, which is called from now on the superstructure, is of concentrically braced frame (CBF) type. In fact, for higher efficiency of the rocking motion in decreasing the seismic response of the superstructure, it should be relatively stiff to facilitate limiting the inter-story drifts. Therefore, moment resisting frames does not seem to be appropriate for this purpose, and CBFs or frames with shear walls are used.

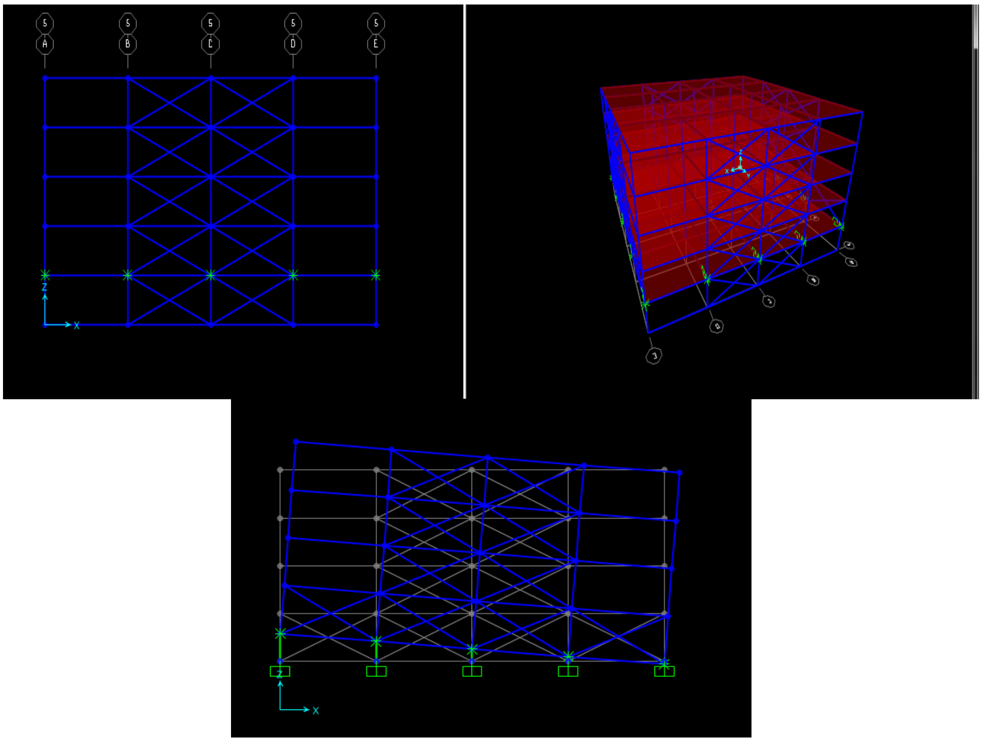

**Fig. 3: The 3-D view of the rocking building and the grid of strong Orthogonal girder and its supporting space truss**

## 3-Numerical Modelling of the CED Device and the Proposed Rocking Building

To assess the realistic hysteretic force-displacement curve of the proposed CED devices, a powerful finite element (FE) program was used, and for verification of the numerical modelling process the results of cantilever beam in large plastic deformation were used as explained in the main report of the study (Alavi 2014) [9]. After verification, by performing a set of FE analyses on CED devices with different sizes of the curved plates their initial (initial) and post-yield (secondary) stiffness values as well as their yielding strength were obtained. The appropriate values of initial and secondary stiffness for the CED device may be found by a series of trial and error analysis for each building system. For this purpose, the CED devices can be modelled as the multi-linear plastic springs in the numerical model of the whole building structure as shown in Figure 3. The initial stiffness of the device affect remarkably the modal periods of the rocking building, and its yield strength and post-yield stiffness control the energy dissipation potential of the system. The CED device stiffness values also affect the values of stress ratio in the superstructure elements, which is on the other side under the effect of the relative stiffness of the grid of the orthogonal strong girders. By assigning different structural properties to both CED device and the grid elements, and observing the stress ratios under the deal and live load of the building decision can be made on the desired values.

## 4-Nonlinear Time History Analyses of the Conventional and base isolation the Proposed Rocking Buildings

For seismic response evaluation of the two designed counterpart buildings a series of nonlinear time history analysis (NLTHA) were performed by using three-component accellorograms of a set of selected earthquake based on their frequency content to be compatible with the considered site condition and the natural periods of conventional, base isolation and rocking buildings. The specifications of the selected earthquakes are given in Table 1, and sample of their response spectra are shown in Figure 4

**Table 1: selected earthquakes used for NLTHA and their pga Values in three main directions**

| Earthquake | PGA (g) | | |
|---|---|---|---|
| | In X direction | In Y direction | In Z direction |
| Imperial Valley | 0.351 | 0.238 | 0.145 |
| Coyote Lake | 0.339 | 0.211 | 0.166 |
| Loma Prieta | 0.367 | 0.322 | 0.294 |
| North Ridge | 0.357 | 0.267 | 0.127 |

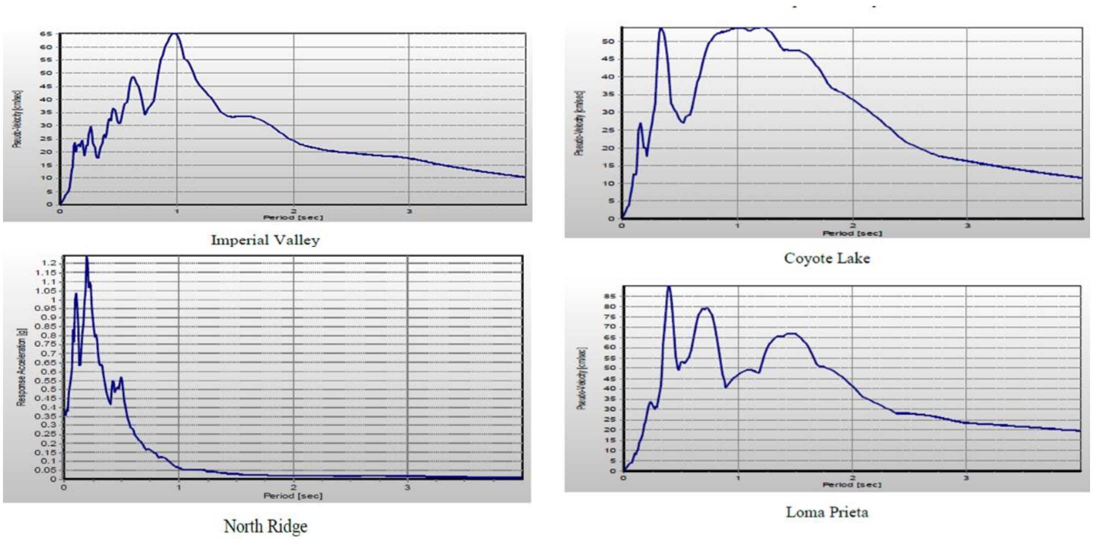


**Fig. 4: Pseudo velocity response spectra, with 5% damping, of the used Earthquakes**

The responses considered for comparison include base shear, roof displacement and acceleration, and inter-story drift of the conventional, base isolation and rocking buildings as well as the hysteresis of the CED devices in the rocking building. The joint at which the aforementioned responses have been extracted from NLTHA, are shown in Figure 5.

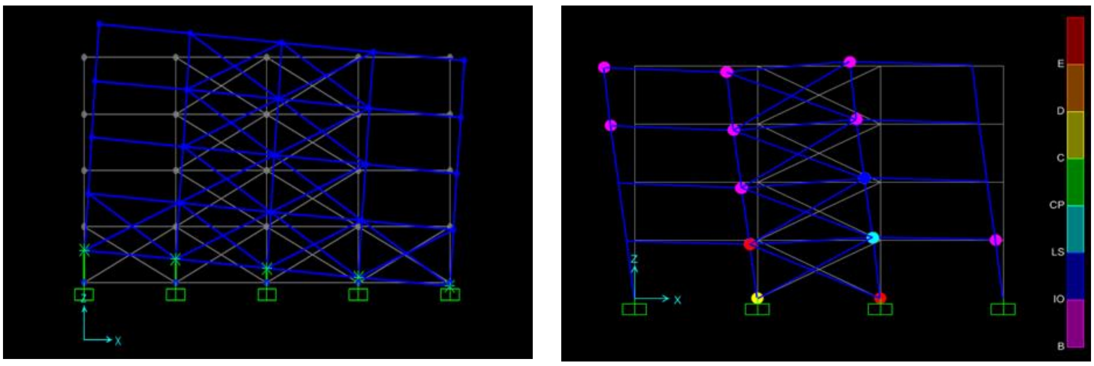

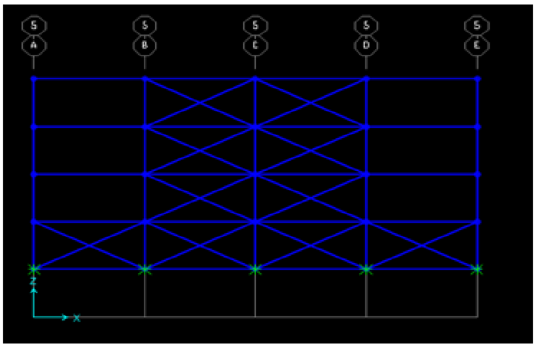

Fig. 4: Comparison of created system in the central frames of the three counterpart buildings subjected to Imperial Valley earthquake

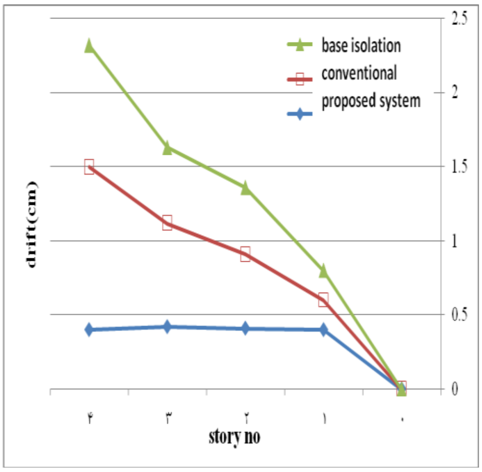


Fig. 5: Comparison of inter-story drifts in the three counterpart buildings Subjected to Imperial Valley earthquake

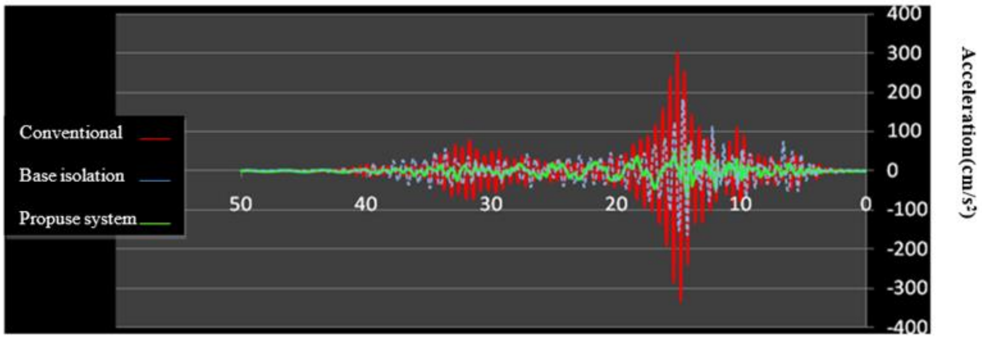


time

Fig.6: Comparison of roof acceleration time histories of the three Counterpart buildings at roof subjected to Imperial Valley earthquake

time

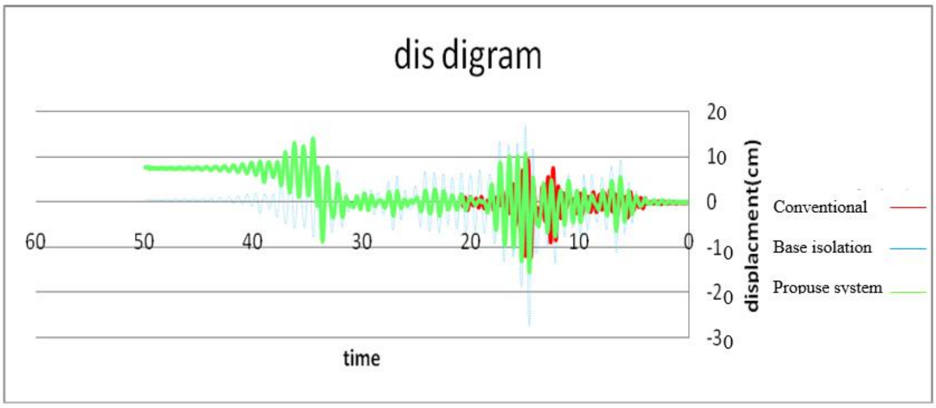


**Fig.7: Comparison of roof displacement time histories of the three Counterpart buildings at joint 7 subjected to Imperial Valley earthquake**

It can be seen in Figures that in the central frame of the conventional building several PHs in the collapse prevention (CP) PL have been formed, while in the counterpart frame of the rocking building no PH has been formed. Also it can be seen in Figures that in the other sample frame of the fixed-base building PHs beyond the CP PL have been formed in several bracing element, which means the collapse of the building. This is while in the counterpart frame of the rocking building only some PHs in immediate occupancy IO PL, and few one in life safety (LS) PL has been formed, and this means that the rocking building can be easily repaired after the earthquake.

## 3- Conclusion

Based on the numerical results obtained from NLTHA of the conventional building and its counterpart rocking building, subjected to several three-component earthquake records, it can be concluded that:

- The suggested structural system leads to a more reliable seismic behaviour of buildings.
- Plastic deformations happen mainly in the CED devices at ground floor, and therefore, in most cases only a few hinges at the IO or LS performance levels appear in other parts of the building structure.
- Considering the advantages of the proposed rocking and energy-dissipating structural system in seismic reduction of mid-rise multi-story buildings, and particularly the easiness of manufacturing and installation of the CED devices, the use of this system can be strongly recommended for buildings in the vicinity of active faults, particularly in large populated cities.

## References

[1] M Hosseini and S Alyasin, "Deliberate Directing of Damage in Lifeline Systems Subjected to Earthquakes," Proceedings of the Hazard-96 Symposium, Toronto, Canada, July 1996.
[2] M Fintel and SK Ghosh, "The Structural Fuse: An Inelastic Approach to Earthquake-Resistant Design of Buildings," Civil Engineering - ASCE, Vol. 51, No. 1, pp. 48-51, January 1981.
[3] R Vargas and M Bruneau, "Seismic Design of Multi-Story Buildings with Metallic Structural Fuses," Proceedings of the 8th U.S. National Conference on Earthquake Engineering (Paper N. 280), San Francisco, California, USA, 18-22 April 2006.
[4] T Azuhata, M Midorikawa and T Ishihara, "Earthquake Damage Reduction of Buildings by Self-Centering Systems Using Rocking Mechanism," Proceedings of the 14th World Conference on Earthquake Engineering, Beijing, China, 2004.

[5] MG Gray, C Christopoulos and JA Packer, “Cast Steel Yielding Fuse for Concentrically Braced Frames,” Proceedings of the 9th U.S. National and 10th Canadian Conference on Earthquake Engineering, Toronto, Canada 25-29 July 2010.
[6] M Hosseini and E Noroozinejad Farsangi, “Seismic Behavior and Performance of Telescopic Columns as a New Base Isolation System for Vibration Control of Multi-Story Buildings,” International Journal of Earthquakes and Structures, Vol. 3, No. 3, December 2012.
[7] M Hosseini and S Bozorgzadeh, “Investigating Double-ADAS Device Behavior and Comparison with ADAS Device,” Proceedings of the International Conference on Earthquake Engineering (SE-50EEE), Skopje, Macedonia, 2013.
[8] M Hosseini and S Kherad, “A Multi-Stud Energy Dissipating Device as the Central Fuse to Be Used in Short- to Mid-Rise Regular Steel Buildings with Rocking Motion,” Proceedings of the International Van Earthquake Symposium, Van, Turkey, October 2013

# Using Multi-objective Simulated Annealing Algorithm to Solve a Multi-objective Facility Layout Problem in Dynamic Cellular Manufacturing

**Navid Darvish Ghaderi[a], Ramezan Nemati Keshteli[b], [c]Pooya Zandkarimi**
[a]M.Sc Industrial Engineering, Mazandaran Institute of Technology, Babol, Iran
[b]Department of Industrial Engineering, Faculty of Engineering-East of Guilan, Guilan university, Vajargah, Iran
[c] Department of industrial engineering, B.Sc Industrial Engineering
* Corresponding author: E-mail address: Navid.dq@gmail.com

**Abstract**
In cellular production, the production system is aimed at transforming several subsystems into a cell in order to produce similar products in a cell with a higher efficiency. In this paper, a multi-objective model in the layout-routing problem of cell production with the goal of minimizing costs, maximizing the level of service to customers has been addressed and solved using the meta-heuristic algorithm MOSA. The results of solving a bi-objective model using this meta-heuristic algorithm with its results in its previous solution method, the meta-heuristic algorithm NSGAII and the Epsilon constraint method showed that MOSA is able to provide better responses than NSGAII for large-scale issues. That is, at approximately equal times, algorithm MOSA was able to produce more accurate and better answers for the second objective function.
**Keywords**: Cellular Production; Multi-objective Model; Meta Heuristic Algorithms; MOSA; NSGAII; Epsilon Constraint

## 1- Introduction

The cell production system is one of the most efficient systems for production environments with high volume and high product diversity. In cellular production, the production system is attempted to transform into several subsystems and indeed cells, in order to produce similar products in a cell with a higher efficiency. Wang et al. [6] for the first time, considered the minimization of intracellular and intracellular transport costs in the cellular model simultaneously and used simulated annealing to solve it. Safaei et al. [8] reviewed the research on cell formation issues in cellular production systems. Saidi et al. [7] used a neural network method to solve the formation problem of the cell with the aim of minimizing the cost of redeployment, fixed cost and machine change, taking into account the multiple paths and repetitions of machines. Mahdavi et al. [9] the mathematical model developed the correct integer for the design of the cell production system, taking into account the factors of labor. Deljo et al. [13] presented a mathematical model for cellular production, and solved it with an improved genetic algorithm. Kia et al. [11] studied a nonlinear mathematical model for designing a cellular production system and used an efficient refrigeration simulation algorithm to solve this problem. Yu and Chen [5] provided a solution to the data structure in optimizing the combined colony algorithm for solving dynamic arrangement problems of large-size facilities. Bozorgi et al. [16] provided a tabu-search algorithm for the problem-setting problem of facility arrangement. Li et al. [10] introduced the dynamic arrangement of facilities, including transportation and material handling, and material re-planning for several production cycles. Mahdavi [4] introduced a multi-objective model for cellular production with the goal of minimizing costs (internal and external cost of transportation, transportation costs, intercellular costs, cost of removal and installation of machine, fixed cost, salary cost, recruitment and dismissal costs, maintenance costs and cost of deficiency) and maximize customer service levels, which is solved using the meta-heuristic algorithm NSGA II. Tavakoli Moghadam et al. [2] presented a model of the production system for dynamic and probable demand, and because of the probability of the model, in addition to considering the goal of minimizing machine costs, repositioning, intra-cellular transport and internal Cells terminated the total penalty deviation from the average demand for the components and solved it by using the simulated annealing algorithm. Imani [1] has proposed a model of dynamic and probable demand cell production system and used a heuristic combination algorithm with simulated annealing algorithm to solve it. Safaei et al. [8] reviewed the papers that considered the dynamics in the cell production system and then, by adding the cost of intracellular and intracellular transport to the model presented in Saidi et al. [7], a new model Provided. The emphasis of the proposed model on the movement of intracellular and intercellular materials with the assumption of the sequence of operations, multiple operational paths and the possibility of repetitions of machines is of a kind in the cell. Kahfi et al [3] function cell formation and production planning. In the proposed algorithm, using the local optimal data and re-setting, the worst particle scattering of the responses increases and prevents early convergence. S. Kirkpatrick [15] has proposed a neighboring search engine widely used to optimize discrete issues. The nature of the decision making algorithm is that for each move, a new neighborhood is generated and evaluated randomly. SA is in fact a robust random search method used to find a good (not necessarily optimal) answer to compound problem issues. In contrast to common search methods, in each replication, in addition to moving to a better answer, answers with a better target function value are accepted with a non-zero probability. SA is inspired by the solid process of cooling the molten material solid. In section 2 of this article, we introduce a multi-objective model presented by Mahdavi[4]. Then, in section 3, the bi-objective model is solved using the MOSA algorithm and the results are compared with the NSGA II in several numerical examples we will describe the results of numerical calculations, and finally in section 4 we will discuss and conclude and present proposals for future work.

## 2- Multi-objective model

In this section, the bi-objective model presented by Mahdavi [4] is introduced. In this model, the assumptions about the fixed cost of each machine include the cost of buying and launching, the machine's variable cost depends on the amount charged to it. In fact, the total fixed costs and variable costs indicate the cost The demand for each piece in each period is variable and it is known that the shift of machines from one cell to another into periods is zero and time is internal and external The cell is clear at all planning horizons, the number of machines is constant during the planning horizon, the salary cost for each worker, regardless of whether it is active or not. The superiority of the worker is clear; it is intended. The flexible path of a piece is defined as a variety of processing programs for each part. The flexibility of the route is the flexibility of the machine and the flexibility of the operation. The machine's flexibility indicates a variety of operations that a machine can do without the need to attempt to change from one operation to another. The flexibility of the operation of a piece, the ability to produce in different ways, is in fact the flexibility of the decision path associated with choosing a path for a piece. The cost involved in choosing a route is called the operating cost expressed in this model.

## 2-1- Indices

| | |
|---|---|
| $p = 1, \dots, P$ | Number of part types. |
| $w = 1, \dots, W$ | Number of worker types. |
| $m = 1, \dots, M$ | Number of machine types. |
| $c = 1, \dots, C$ | Number of cells types. |
| $t = 1, \dots, T$ | Number of periods. |
| $j = 1, \dots, J$ | Number of operations types. |

## 2-2- Input parameters

| | |
|---|---|
| $D_{pt}$ | Demand of part type $p$ in period $t$. |
| $B_p^{inter}$ | batch size for inter-cell movements of part batch *p*. |
| $B_p^{intra}$ | batch size for intra-cell movements of part *p*. |
| $\gamma^{inter}$ | Inter-cell movement cost per batch. |
| $\gamma^{inter}$ | Intra-cell movement cost per batch. |
| $x_m$ | constant cost of machine type *m*. |
| $y_m$ | variable cost of machine type *m*. |
| $L_{cm}$ | Minimum size of cell *c* in terms of the number of machine types. |
| $U_{cm}$ | Maximum size of cell *c* in terms of the number of machine types. |
| $L_{cw}$ | Minimum size of cell *c* in terms of the number of workers. |
| $U_{cw}$ | Maximum size of cell *c* in terms of the number of workers. |
| $f_m$ | The number of available machines of type *m*. |
| $f_w$ | The number of available workers of type *w*. |
| $\alpha_p$ | Unit holding cost of part type p in period *t*. |
| $\beta_p$ | Unit backorder cost of part type p in period *t*. |
| $T_{wt}$ | Available time for worker type *w* with in period *t*. |
| $T_{mt}$ | Available time for machine type *m* in period *t*. |
| $t_{pmw}$ | Processing time of part type *p* on machine type *m* with worker type *w*. |
| $e_m$ | Installing cost of machine type *m*. |
| $d_m$ | Removing cost of machine type *m*. |
| $S_{wt}$ | Salary cost of worker type *w* with in period *t*. |
| $H_{wt}$ | Hiring cost of worker type *w* with in period *t*. |
| $F_{wt}$ | Firing cost of worker type *w* with in period *t*. |
| $A$ | An arbitrary big positive number. |

## 2-3- Decision variables

| | |
|---|---|
| $z_{mct}$ | Number of machines of type *m* allotted to cell *c* in period *t*. |
| $z_{wct}$ | Number of workers of type *w* allotted to cell *c* in period *t*. |
| $R^{+}_{mct}$ | Number of machines of type *m* added to cell *c* during period *t*. |
| $R^{-}_{mct}$ | Number of machines of type *m* removed from cell *c* during period *t*. |
| $x_{jpmwct}$ | 1 if operation type *j* on part *p* is to be processed on machine type *m* with worker *w* in cell *c* in period t;=0 otherwise. |
| $Q_{pt}$ | Production volume of part type *p* to be produced in period *t*. |
| $L^{+}_{wct}$ | Number of workers of type *w* added to cell c during period *t*. |
| $L^{-}_{wct}$ | Number of workers of type *w* removed from cell c during period *t*. |
| $I^{+}_{pt}$ | Inventory of part type *p* at the end of period t, $I^{+}_{p0} = 0$. |
| $I^{-}_{pt}$ | Backorder of part type *p* in period t, $I^{-}_{p0} = 0$. |

## 2-4- Mathematical model

$$\text{Min } z_1=\frac{1}{2}\sum_{j=1}^{J}\sum_{p=1}^{P}\sum_{w=1}^{W}\sum_{c=1}^{C}\sum_{t=1}^{T}\left\lceil\frac{Q_{pt}}{B_p^{\text{inter}}}\right\rceil\gamma^{\text{inter}}\left|\sum_{m=1}^{M}x_{(j+1)pmwct}-\sum_{m=1}^{M}x_{jpmwct}\right|$$

$$+\frac{1}{2}\sum_{j=1}^{J}\sum_{p=1}^{P}\sum_{w=1}^{W}\sum_{c=1}^{C}\sum_{t=1}^{T}\left\lceil\frac{Q_{pt}}{B_p^{\text{inter}}}\right\rceil\gamma^{\text{intra}}\left(\sum_{m=1}^{M}\left|x_{(j+1)pmwct}-x_{jpmwct}\right|-\left|\sum_{m=1}^{M}x_{(j+1)pmwct}-\sum_{m=1}^{M}x_{jpmwct}\right|\right)$$

$$+\sum_{m=1}^{M}\sum_{c=1}^{C}\sum_{t=1}^{T}e_m R^{+}_{mct}+\sum_{m=1}^{M}\sum_{c=1}^{C}\sum_{t=1}^{T}d_m R^{-}_{mct}+\sum_{m=1}^{M}\sum_{c=1}^{C}\sum_{t=1}^{T}x_m Z_{mct}$$

$$+\sum_{j=1}^{J}\sum_{p=1}^{P}\sum_{m=1}^{M}\sum_{w=1}^{W}\sum_{c=1}^{C}\sum_{t=1}^{T}y_m Q_{pt}t_{pmw}x_{jpmwct}+\sum_{w=1}^{W}\sum_{c=1}^{C}\sum_{t=1}^{T}s_{wt}Z_{wct}$$

$$+\sum_{w=1}^{W}\sum_{c=1}^{C}\sum_{t=1}^{T}L^{+}_{wct}H_{wt}+\sum_{w=1}^{W}\sum_{c=1}^{C}\sum_{t=1}^{T}L^{-}_{wct}F_{wt}+\sum_{p=1}^{P}\sum_{t=1}^{T}(\beta_p I^{-}_{pt}+\alpha_p I^{+}_{pt}) \qquad (1)$$

$$\text{Max } z_2=\frac{\sum_{p=1}^{P}\sum_{t=1}^{T}Q_{pt}}{\sum_{p=1}^{P}\sum_{t=1}^{T}D_{pt}} \qquad (2)$$

$$\sum_{p=1}^{P}\sum_{m=1}^{M}x_{jpmwct}t_{pmw}Q_{pt}\le Z_{wct}T_{wt} \qquad \forall w,t,c,j \qquad (3)$$

$$\sum_{p=1}^{P}\sum_{w=1}^{W}x_{jpmwct}t_{pmw}Q_{pt}\le Z_{mct}T_{mt} \qquad \forall m,t,c,j \qquad (4)$$

$$\sum_{m=1}^{M}\sum_{w=1}^{W}\sum_{c=1}^{C}x_{jpmwct}\le AQ_{pt} \qquad \forall p,t \qquad (5)$$

$$D_{pt} = Q_{p,t} + I^{+}_{p(t-1)} - I^{-}_{p(t-1)} - I^{+}_{pt} + I^{-}_{pt} \qquad \forall p,t \qquad (6)$$

$$Z_{mct} = Z_{mc(t-1)} + R^{+}_{mct} - R^{-}_{mct} \qquad \forall m,c,t \qquad (7)$$

$$\sum_{c=1}^{C} Z_{mct} \le f_{m} \qquad \forall m,t \qquad (8)$$

$$\sum_{m=1}^{M} Z_{mct} \ge \sum_{m=1}^{M} L_{cm} \qquad \forall c,t \qquad (9)$$

$$\sum_{m=1}^{M} Z_{mct} \le \sum_{m=1}^{M} U_{cm} \qquad \forall c,t \qquad (10)$$

$$Z_{wct} = Z_{wc(t-1)} + L^{+}_{wct} - L^{-}_{wct} \qquad \forall c,\mathrm{w},t \qquad (11)$$

$$\sum_{c=1}^{C} Z_{wct} \le f_{w} \qquad \forall w,t \qquad (12)$$

$$\sum_{w=1}^{W} Z_{wct} \ge \sum_{w=1}^{W} L_{cw} \qquad \forall c,t \qquad (13)$$

$$\sum_{w=1}^{W} Z_{wct} \le \sum_{w=1}^{W} U_{cw} \qquad \forall c,t \qquad (14)$$

$$Z_{mct}, Z_{wct}, R^{+}_{mct}, R^{-}_{mct}, L^{+}_{wct}, L^{-}_{wct}, Q_{pt} (\mathrm{int}eger) \\ I^{+}_{pt}, I^{-}_{pt} \ge 0 \qquad (15)$$

$$x_{jpmwct} \in \{0,1\} \qquad (16)$$

Equation (1) represents the objective function, which involves minimizing various costs, the first part of which represents the cost of intercellular transport, and the second part represents the cost of transport, intracellular, part three and fourth Indicates the cost of installing and removing machines, which represents the cost of re-engineering. Section 5 and 6 are fixed and variable costs of machines, the total of which represents operating costs. Section 7 illustrates the wage bill, Section 8 and 9, indicating the cost of recruiting and dismissing, Section 10 and Eleventh shows cost of maintenance and shortage. Equation (2) it shows the second objective function is to maximize the level of service to the customer, which ultimately increases customer satisfaction. Equation (3) and (4) indicate that production capacity should not exceed the capacity of the machine and worker in the production system. Equation (5) shows that if the production volume is zero, there is no worker and machine to produce the piece. Equation (6) expresses the equilibrium of the number of demands in each period. Equation (7) expresses the balance of machines. Equation (8) states that the total number of machines per cell should not exceed the total number of machines available. Equation (9) and (10) indicate the upper and lower limits of the cell based on the number of machines. Equation (11) shows the balance of the number of workers in each period. Equation (12) indicates that the capacity of the number of workers in each cell should not be greater than the total number of workers available. Equation (13) and (14) express the upper and lower limit of the number of workers assigned to each cell. Equation (15) and (16) represent the values of the decision variables.

## 3- Computational results

The proposed model in the second part is solved in seven examples using the optimal solution of multi-objective models, epsilon constraints, and also by the two meta-heuristic methods, MOSA [15] and NSGA II [14]. The values of the bi-objective model parameters are presented in Table 1.

**Table 1. The values of the bi-objective model parameters**

| parameter | Range | parameter | range |
|---|---|---|---|
| $D_{pt}$ | [3,8] | $f_w$ | 2 |
| $\alpha_p$ | [100,200] | $T_{wt}$ | 1 |
| $\beta_p$ | [100.200] | $T_{mt}$ | 2 |
| $B_p^{\text{inter}}$ | [5,14] | $\gamma^{inter}$ | 50 |
| $B_p^{intra}$ | [10,15] | $\gamma^{intra}$ | 100 |
| $t_{pmw}$ | [0,5.3] | $d_m$ | 250 |
| $e_m$ | [150,200] | $H_{wt}$ | 40 |
| $x_m$ | [75.125] | $L_{cm}$ | 1 |
| $f_m$ | [2,3] | $U_{cm}$ | 2 |
| $y_m$ | [150,200] | $L_{cw}$ | 1 |
| $F_{wt}$ | 20 | $U_{cw}$ | 2 |
| $A$ | M | $S_{wt}$ | 300 |

The results are presented in 7 examples of the problem in three ways in Table 2. Each problem is solved in meta-heuristic algorithms 10 times and the average results are reported, as well as the Epsilon value is 24. The Taguchi experimental design method was used to adjust the parameters of the meta-heuristic methods. The number of members of the population was 20 and the number of iteration was 150. In method NSGAII, the probability of mutation was equal to 0.1 and the probability of reproduction was equal to 0.9. In method MOSA, the values of Primary temperature, Temperature parameter were obtained based on the formulas presented in the S. Kirkpatrick [15] paper.

**Table 2. Bi-objective model solving results**

| Method | Index | Values | | | | | | |
|---|---|---|---|---|---|---|---|---|
| | J | 2 | 2 | 4 | 4 | 6 | 6 | 6 |
| | P | 2 | 2 | 3 | 4 | 4 | 5 | 5 |
| | M | 2 | 3 | 3 | 3 | 3 | 3 | 4 |
| | W | 2 | 3 | 2 | 2 | 3 | 2 | 2 |
| | C | 3 | 2 | 3 | 2 | 2 | 4 | 2 |
| | T | 2 | 2 | 2 | 4 | 2 | 2 | 3 |
| Epsilon Constraint Method | F1 | 9470 | 12760 | 30230 | 41108 | 105841 | Error | Error |
| | F2 | 1 | 1 | 1 | 1 | 1 | Error | Error |
| | Total time (s) | 3 | 5 | 11 | 18 | 717 | 3600 | 3600 |
| NSGAII Method | F1 | 10270 | 13001 | 31116 | 41912 | 106714 | 225413 | 341560 |
| | F2 | 0.20 | 0.31 | 0.23 | 0.15 | 0.39 | 0.52 | 0.41 |
| | Total time (s) | 12 | 23 | 33 | 57 | 129 | 325 | 493 |
| MOSA Method | F1 | 10452 | 13099 | 31312 | 42261 | 106818 | 225640 | 342198 |
| | F2 | 0.53 | 0.39 | 0.37 | 0.38 | 0.44 | 0.45 | 0.52 |
| | Total time (s) | 14 | 26 | 39 | 62 | 137 | 332 | 500 |

The Epsilon constraint method has been able to solve the corresponding model only in small-dimensional problems. Seven different problems were selected to distinguish the superstring algorithms in comparing the model with the Epsilon constraint method. Two meta-heuristic algorithms do not differ much in terms of the time of solving the model. In the results, we see that the meta-heuristic algorithm NSGAII provides better values for the first objective function than the MOSA meta-heuristic algorithm, but this difference is negligible, but the values generated for the second objective function in the MOSA method are much better than the NSGAII method. Also, by increasing the dimensions of the problem, the precision of the MOSA method is not diminished to determine the values of the objective functions, and it can be clearly seen that the uniformity of the Pareto responses in this algorithm is much greater than the NSGAII algorithm for the second-objective function.

## 3-1- Pseudo code of Algorithms

The Pseudo code related to the meta-heuristic algorithms are presented in Table 4

**Table 3. Pseudo code of the meta-heuristic algorithms**

*MOSA*

```
if dominate(newpop.fit,bestnewpop.fit)
% bestnewpop=best new pop
bestnewpop=newpop;
end
end
if dominate(bestnewpop.fit,pop(i).fit)
pop(i)=bestnewpop;
else
E=bestnewpop.fit-pop(i).fit;
Pr=exp(-E/T);
if all(rand<Pr)
pop(i)=bestnewpop;
```

*NSGAII*

```
% crossover
crosspop=repmat(emp,ncross,1);
crosspop=crossover(crosspop,pop,ncross,data,F);

% mutation
mutpop=repmat(emp,nmut,1);
mutpop=mutation(mutpop,pop,nmut,data,F);
[pop]=[pop;crosspop;mutpop];
```

## 4- Conclusion

In this paper, a bi-objective model for the Facility Layout problem with the aim of minimizing the cost function and maximizing the level of service has been considered. The model has been solved using the MOSA meta-heuristic algorithm. There are different metrics for the comparison of meta-heuristic algorithms. In this paper, the criterion of the time of solving and producing Pareto-quality responses was considered for the objective functions. The results of the model solving showed that MOSA meta-heuristic algorithm can perform better than NSGAII meta-heuristic algorithm in solving a larger-dimensional model. The values generated for the second objective function in the MOSA method are much better than the NSGAII method. From the results obtained, it can be seen that accurate exact solution algorithms are suitable for small-scale problems and do not have the ability to solve large problems. The meta-heuristic algorithms with the ability to generate nearly optimal Pareto answers, showed their efficiency in solving large-scale problems. For future work, Different issues are solved with different algorithms and their results are compared with each other. Considering uncertainty in the parameters that are expected, such as demand, can also be considered in subsequent research.

## References

[1]. Imani Eini M, 2003, Master's thesis, Department of Industrial Engineering, University of Tehran, Designing of Cellular Systole in Dynamic and Positive Demand and Solving It Using An Effective Inventive Method, p.7-36.

[2]. Tavakoli Moghadam, Javadian, 2002, 2nd National Conference of Industrial Engineering, Yazd University, Designing a Cell Production System under Possible Dynamic Conditions and Solving it by SA, p. 29-30.

[3]. Kahfi A., Barzinpour, Tavakoli Moghadam, 2012, Industrial Engineering Journal, Development of Particle Mass Optimization Algorithm for Solving the Integrated Model of Production Planning and Dynamic Cell Production System, p. 77.

[4]. Mahdavi, 2015, Master thesis, Industrial Engineering Department, Mazandaran Industrial Institute, Problem of routing layout in dynamic cell production, p. 70.

[5].Yu G, Chen H, 2013, A new data structure of solution representation in hybrid ant colony optimization for larg dynamic facility layout problems, International Journal of Production Economic p. 362-371.

[6].Wang T.Y, Wu K.B, Liu Y.W, 2001, A Simulated annealing algorithm for facility layout problems under variable demands in cellular manufacturing system, Computer in Industrial, vol.46, p. 181-188.

[7].Saidi-mehrabad M,Safaie N, 2007, A new model of dynamic sell formation by a neural approach, International journal Advance Manufacturing Technology, vol.33, p 1001–1009

[8].Safaei N, Saidi M.Mehrabad M.S, 2008, A hybrid simulated annealing for solving an extended model of dynamic cellular manufacturing system, Europeanjornal of operational research, vol. 185, p. 563-592.

[9].Mahdavi I, Aalaie A, Paydar M.M, Solimanpur M, 2010, designing a mathematical model of dynamic cellular manufacturing systems considering production planning and worker assignment, Computer and Mathematics with Applications, vol.60, p.1014-1025.

[10].Li L, Li B, Liang H, Zhu W, 2014, The Heuristic Methods of Dynamic Facility Layout Problem, Advances in Intelligent Systems and Computing, volume 214, p. 269-278.– 25.

[11].Kia R, Baboli A,Javadian N, Tavakoli-Moghadam R, Kazami M, Khorami J, 2012,Solving a group layout design model of a dynamic cellular manufacthuring system with alternative process routings, Computers & Operation Research, vol39,p. 2642-2658.

[12].Haimes, Y.Y. and Lasdon, L.S. and Wismer, D.A, 1971, on a bicriterion formulation of the problems of integrated system identification and system optimization, IEEE Transactions on systems, Man and Cybernetics,vol.1, p.296-297.

[13].Deljo V, Mirzapor S.M.J, Hasem A, Deljo F, Aryanezhad M.B, 2010, genetic algorithm to solve dynamic cell formation problem , Applied Mathematical Modeling, vol.34, p.1078-1092.

[14]. K. Deb; A. Pratap, S. Agarwal, T. Meyarivan, 2002, A fast and elitist multi-objective genetic algorithm, IEEE Transactions on Evolutionary Computation, Vol.6, p.182-197.

[15]. S. Kirkpatrick; C. D. Gelatt; M. P. Vecchi, 1983, Optimization by simulated annealing, Science, vol, 220, p.671-680.
[16]. Bozorgi N, Abedzadeh M, Zeinali M, 2012 , Tabu search heuristic for efficiency of dynamic facility layout, International Journal Of Advanced Manufacturing Technology, vol.77, p 689–703.

# A low-phase noise source injection-coupled LC quadrature oscillator with tail noise filter

**Marzieh Chaharboor *, Saman Mokhtabad, Hojat Ghonoodi**

*1. Graduate student of Electrical and Electronics Engineering, Marzieh.Chaharboor@gmail.com*
*2. Graduate student of Electrical and Electronics Engineering, Saman.Mokhtabad@gmail.com*
*3. PhD of Electrical and Electronics Engineering, h.ghonoodi@gmail.com*

**Abstract**

This paper presents a low phase noise source injection coupled quadrature oscillator (IC-QO). Like most of the works which have been presented for parallel coupled quadrature oscillators (PC-QO), the presented IC-QO using passive components like capacitance instead of noisy active devices with casualties for coupling the oscillator circuits that lead to elimination of the phase noise due to the coupling transistors. The presented IC-QO also uses the re-filtering technique of the sideband noise. Furthermore, the second harmonic of the tail current source suppressed by creating high impedance in the tail, which applied for the proposed IC-QO to be more noiseless. Reducing the noise frequencies around $2\omega_0$, leads to the amplitude of quadrature signals become larger and also the phase noise reaches to the lowest possible amount of noise level. To confirm, a 3.4 GHz proposed design of CMOS source injection coupled quadrature oscillator with LC noise filter structure in the tail is simulated. Using 0.18µm TSMC CMOS technology proved that the proposed structure with passive components and using LC filter shunted with tail current source exhibit a low phase noise of -157 dBc at 3MHz offset frequency and -187.2 dBc at 3GHz frequency. The obtained results show the agreement.

**Key words:** Injection Coupled, LC Quadrature Oscillator, RF CMOS, Passive Components, Phase Noise, Tail Noise Filter.

## 1. Introduction

Due to the demand for low cost, small form factor scale and large scale integration of system-on-chip (SoC) wireless transceivers, the image-reject, zero-IF and low-IF receiver architectures have become the main topologies used in mainstream wireless communication systems [1].

The performance of wireless communication systems is strongly depending on the quality of quadrature oscillator (QO). The most significant performance measures of QOs are phase noise, phase error and power consumption [2] which have major impacts on the overall receiver efficiency. There are several different methods to produce quadrature outputs such as RC-CR methods, polyphase filters [3], even-stage ring oscillators [4] and LC QOs. Among these methods, LC tank QOs are attractive, due to their low phase noise [5-9].These types of QOs usually consist of two coupled LC oscillators.

Different methods have been proposed to couple two CMOS LC tank oscillators. The first method is the parallel coupled QO (PC-QO), proposed by A.Rofougaran [10]. Series coupled QO (SC-QO) and source injection coupled QO (IC-QO) are other LC-tank quadrature oscillators. To achieve lower phase noise, SC-QO has been instructed [11] and based on [12-15], it can be concluded that IC-QO has lower phase noise than the others.

In this paper, a new structure of source injection coupled QO has been proposed in which the noiseless passive components in lieu of noisy active coupling devices. In addition to using noiseless passive coupling devices, applying re-filtering technique leads to more desirable phase noise. Also, additional LC filter in the tail of switching transistors results to attractive achievement in order to improve the phase noise performance. With the proper conception of phase noise can understand that adding passive LC filter can reduce the phase noise factor of LC quadrature oscillators and its minimum value can be reached. The proposed structure uses this conception to obtain a better phase noise. The organization of this paper is as follows: In the section 2, the basic outlines of source injected QOs are explained and in section 3 the proposed IC-QO structure which provides a new IC-QO configuration using additional tail noise filter is presented. In the following in section 4, to evaluate the proposed source injected QO, a 3.4 GHz QO is simulated and the results are provided. Finally in section 5, the conclusion summarizes achievements of the presented idea of this paper.

## 2. Source Injection Coupled Quadrature Oscillator (IC-QO)

Passing two differential outputs at frequency of $2\omega_0$ through a frequency divider is a conventional method of generating quadrature outputs at frequency of $\omega_0$.The basic of this method is very simple. The two differential outputs have a phase difference of 180° and therefore dividing them by 2 generates two signals with phase difference of 90° [16]. The outputs of two oscillators with sinusoidal opposite phase tail currents at frequency of $2\omega_0$ will be quadrature signals of frequency of $\omega_0$ [13]. Figure 1 shows such a mentioned circuit in which signals at frequency of $2\omega_0$ are fed to cross-coupled transistors through the source node. Since the cross-coupled transistors are switched by output waveforms. Consequently, the source injected current is multiplied by a square wave at frequency of $\omega$, so the drain currents have two components at frequencies of $2\omega_0+\omega$ and $2\omega_0-\omega$.Since the resonation frequency of LC tank is about $\omega_0$, the frequency component of $2\omega_0+\omega$ doesn't create significant voltage on LC tank so the frequency of output voltage is $2\omega_0-\omega$ [2].

Indeed, the cross-coupled differential-voltage-controlled oscillators operate as frequency divider for the signals injected at the common source node. A drawback of this circuit is that it needs an external oscillator of frequency of $2\omega_0$. In another method, there isn't any external oscillator, and the waveforms of frequency $2\omega_0$ are generated from the outputs of the two coupled LC oscillators. This coupling is performed in several approaches [2].

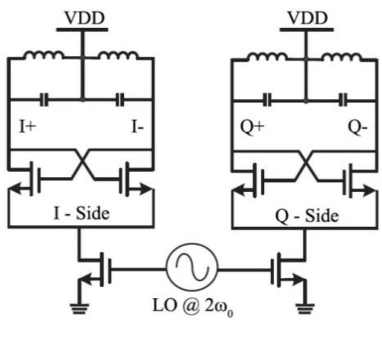


**Figure 1 : An injection QO with an external oscillator**

In the other approach, transistor coupling networks are placed in parallel to switching pairs similar to PC-QO. Figure 2 shows injection coupling mechanism with NMOS [16] and PMOS coupling networks [15].

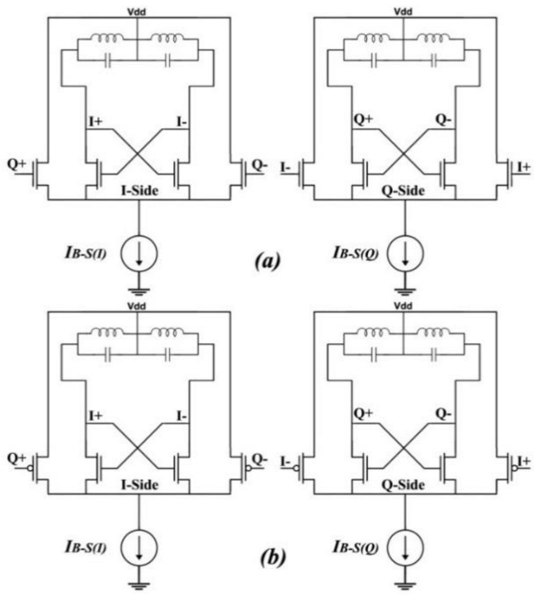


**Figure 2 : Injection coupling mechanism a) NMOS Coupling and b) PMOS Coupling**

The IC-QO mechanism can be considered as a combination of two frequency dividers and two frequency doublers so that the coupling transistor pairs operate as a frequency doubler. However, NMOS and PMOS coupling networks in the IC-QO have similar mechanism, but PMOS coupling network has several advantages over NMOS coupling network. The most significant point is that there is not any current sharing at the source [2].

The schematic of IC-QO with parallel PMOS coupling transistors instead of the external oscillator for injection coupling network is illustrated in Figure 3 which $M_{cp1}$ and $M_{cp2}$ are coupling transistors. These two transistors generate current with frequency of 2ω, twice of QO's oscillation frequency and inject it into the source $M_{sw1}$ and $M_{sw2}$ as oscillation core. The injected current through the source is switched with frequency of ω in switching pairs [2].

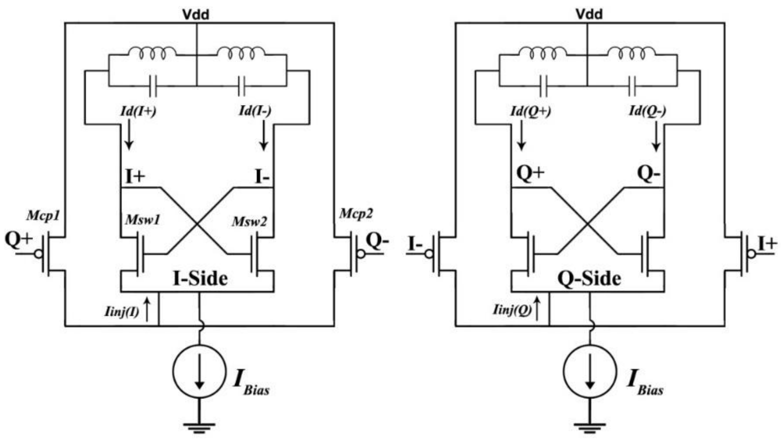


**Figure 3 : The schematic of IC-QO with parallel PMOS coupling transistors**

Additionally, injection current of source capacitor affects the output. The amplitude of this current is $2\omega.C.V_S$ where $\omega$, C and $V_S$ are oscillation frequency, capacitance and source voltage amplitude, respectively. Considering this current makes the analysis more accurate. The drain current of transistors consists of three independent currents; bias, injection and capacitor currents [2].

An overview of the IC-QO structure has been described in this section. In previous works, the uses of passive components in order to couple the switching pairs have been done just on the PC-QO structures [17]. But in this case of study, the IC-QO with passive components which applied for coupling mechanism has been considered. The following section describes the proposed coupled LC quadrature oscillators properly with passive devices which make the quadrature output signals and phase noise more desirable and improved.

## 3. The proposed IC-QO structure

As mentioned before and clearly depicted in the schematic of IC-QO in Figure 3, $M_{cp1}$ and $M_{cp2}$ are used as coupling transistors which degrade the phase noise. So, in order to alleviate the phase noise due to coupling transistors, the proposed idea offers using noiseless passive components like capacitors $C_p$, as applied for coupling in the previous presented PC-QOs to couple the two identical LC-tank oscillators for coupling mechanism.

Since, the passive components have no extra noise and capacitors are noiseless, for the goal of decreasing phase noise, four identical capacitors ($C_p$) are being used for coupling network. To perform the coupling by this capacitive technique, the core of LC oscillators must be modified such as output nodes (I+ and I- or Q+ and Q-). The direct connection of quadrature outputs, while synchronized, leads to the two oscillators oscillate at the same time and in this condition the outputs are not in quadrature. Therefore, the outputs of quadrature oscillators are not injected directly together. As shown in Figure 4 in order to avoid direct connection of output nodes, the capacitor $C_c$ is placed to separate the connection between gate and drain of each oscillator's core. The AC connection of cross-coupled oscillators is provided by these capacitors ($C_c$) and also, they block the DC connection. An inductor ($L_c$) is used in parallel with $C_c$ which provides the appropriate DC bias for the gate of cross-coupled transistors properly. Consequently, the parallel inductor is connected to the capacitor $C_c$ causes the requirement for the extra biasing circuit is eliminated. The values of $L_c$ and $C_c$ should be chosen with considering oscillation frequency of oscillators and they also behave the same as a band-pass filter which uses re-filtering technique to remove the side-band noise of outputs.

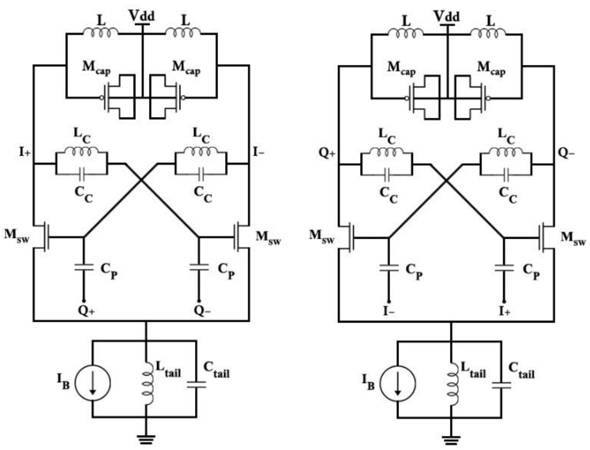


**Figure 4 : The schematic of proposed IC-QO structure with tail noise filter**

To decrease the phase noise, one additional tail noise filter at the source of the IC-QO is offered and this causes the quadrature LC oscillator to be more noiseless. A capacitor ($C_{tail}$) is placed in parallel with the current source and shortens the noise frequency around $2\omega_0$ to the ground. Then, in order to raise the impedance, one inductor ($L_{tail}$) is inserted between the current source and the capacitor in the tail. Obviously, can say an LC filter is placed at the tail. Although, the impedance at the tail can be limited only by the quality factor of the inductor but the values of these two passive components must be chosen accurately by considering the resonation at $2\omega_0$.

## 4. Simulation Results

Based on provided description about proposed IC-QO structure along with tail noise filtering, the configuration of Figure 4 is simulated in Agilent ADS simulator with 0.18µm TSMC CMOS technology. The circuit parameters include active and passive components are listed in Table 1. The inductor's quality factor is considered Q=15.

**Table1: Circuit parameters**

| | |
|---|---|
| $V_{dd}$ | 1.8V |
| $M_{sw}$ (W/L) | 6µm/0.18µm |
| $M_{cap}$ (W/L) | 100µm/0.18µm |
| $C_p$ | 0.5pF |
| $C_C$ | 1pF |
| $L_C$ | 1nH |
| L | 1nH |
| $C_{tail}$ | 0.213pF |
| $L_{tail}$ | 2.3077nH |
| $I_B$ | 1mA |

The result of simulation shows that a desirable phase noise is achieved by using proposed structure. Using an LC tail noise filter improved the performance of phase noise in compare of previous works [17]. As shown in Figure 5, the phase noise of this work at 3MHz offset frequency is -157 dBc and -187.2 dBc at 3GHz frequency.

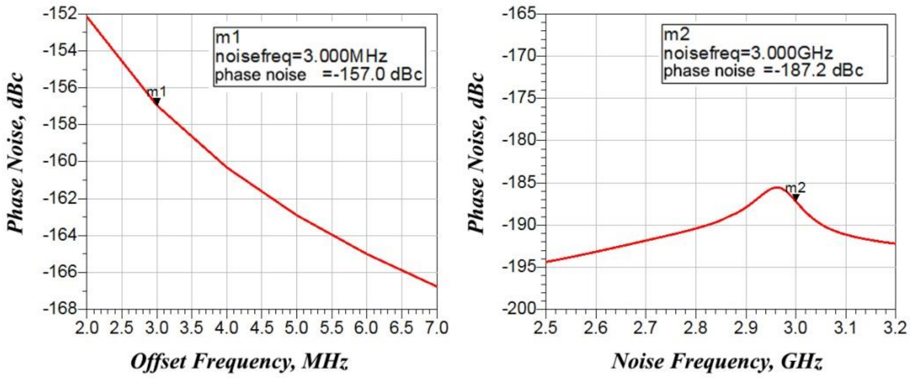


**Figure 5 : Simulated phase noise at 3MHz offset frequency and 3GHz frequency**

The quadrature outputs have quite enough high amplitude which can be another aspect of the proposed idea. The well-known phase noise model for an oscillator is Leeson's proportionality [18] in equation (1) which reveals the dependency of the phase noise upon the signal amplitude $V_O$.

$$L\{\Delta\omega\} \propto \frac{1}{V_O^2}.\frac{kT}{C}.\left(\frac{\omega_0}{Q}\right)^2.\frac{1}{\omega_m^2} \tag{1}$$

With good signal amplitude, it is possible to overcome the phase noise and limit the effects on the phase and get an appropriate performance. Figure 6 illustrates the I-side and the Q-side output waveforms.

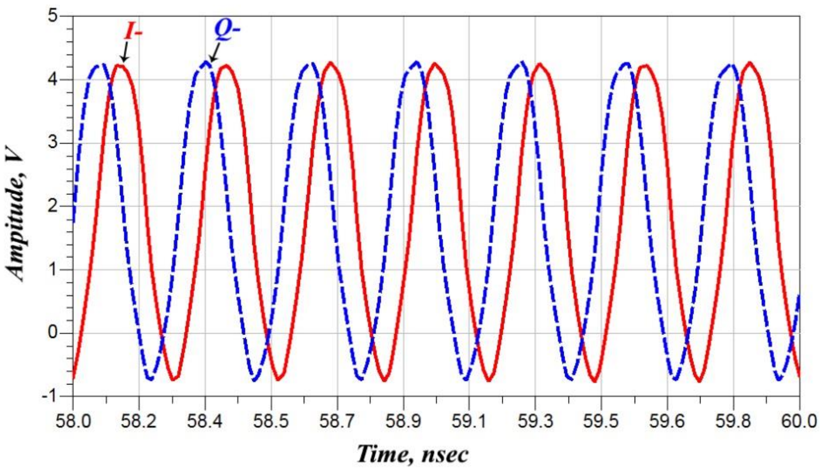


**Figure 6 : The I-Side and the Q-Side quadrature outputs**

## 5. Conclusion

Quadrature oscillators play a critical role in modern wireless communication systems and RF standards. The study of this paper concentrates on the new structure of source injection coupled LC quadrature oscillator by using passive components. The passive components have been used for coupling network and the tail noise filtering technique. In the offered structure, the passive coupling network in collaboration with LC tail filter leads to improve the phase noise performance and provides suitable amplitude in the proposed IC-QO structure. The measured phase noise and amplitude in this structure relatively have desired value. Re-filtering the side-band noise alongside good amplitude and using the LC filter in parallel with the current source in the tail, improve the quadrature outputs from the perspective of the phase noise performance. In comparison with previous works which have been done; this structure according to the mentioned statements and simulation results is favorable.

## References

[1] Rudell, Jacques C., et al. "Recent developments in high integration multi-standard CMOS transceivers for personal communication systems. Proceedings of the 1998 international symposium on Low power electronics and design. Vol. 10. No. 12. 1998.

[2] Ghonoodi, Hojat, and Hossein Miar-Naimi. "Phase error analysis in CMOS injection-coupled LC quadrature oscillator (IC-QO)." International Journal of Circuit Theory and Applications 42.11 (2014): 1123-1138.

[3] Behbahani, Farbod, et al. "CMOS mixers and polyphase filters for large image rejection." Solid-State Circuits, IEEE Journal of 36.6 (2001): 873-887.

[4] Ma DK, Long JR. A subharmonically injected LC delay line oscillator for 17-GHz quadrature LO generat. IEEE Journal of Solid-State Circuits Sep. 2004; 39:1434–1445.

[5] Rofougaran A, Rael J, Rofougaran M, Abidi A. A 900 MHz CMOS LC-oscillator with quadrature outputs. in IEEE Int. Solid State Circuits Conf. (ISSCC) Dig. Tech. Papers, 1996; 392–393.

[6] Mazzanti A, Member A., Svelto F, Andreani P. On the Amplitude and Phase Errors of Quadrature LC-Tank CMOS Oscillators. IEEE Journal of Solid-State Circuits June 2006; 41(6).

[7] Chamas IR, Raman S A Comprehensive Analysis of Quadrature Signal Synthesis in Cross-Coupled RF VCOs. IEEE Transactions on Circuits and Systems I April 2007; 54(4).

[8] Djurhuus T, Krozer V, Vidkjaer J, Johansen T. Nonlinear Analysis of a Cross-Coupled Quadrature Harmonic Oscillator. IEEE Transactions Circuits and Systems I Nov 2005; 52(11):2276–2285.

[9] Romano L, Levantino S, Bonfanti A, Samori C, Lacaita A. Phase Noise and Accuracy in Quadrature Oscillators. In Proc. Int. Symp.Circuits and Systems, 2004; 161–164.

[10] Mirzaei A, Heidari ME, Bagheri R, Chehrazi S, Abidi A. The Quadrature LC Oscillator: A Complete Portrait Based on Injection Locking. IEEE J. Solid-State Circuits Mar. 2007; 42(9).

[11] Andreani P, Bonfanti A, Romanò L., Samori C. Analysis and Design of a 1.8-GHz CMOS LC Quadrature VCO. IEEE J. Solid-State Circuits Dec. 2002; 37(12).

[12] Rategh HR, Lee TH. Superharmonic injection-locked frequencydividers. IEEE Journal of Solid-State Circuits June 1999; 34:813–821.

[13] Cabanillas J, Dussopt L, López-Villegas JM, Rebeiz GM. A900 MHz low phase noise CMOS quadrature oscillator. in Proc. IEEE RFIC Symp., 2000; 63–66.

[14] Choi HC, Shin SB, Lee SG A Low-Phase Noise LC-QVCO in CMOS Technology. IEEE Microwave and Wireless Components Nov. 2004; 14(11).

[15] Chamas IR, Raman S. Analysis and Design of a CMOS Phase-Tunable Injection-Coupled LC Quadrature VCO (PTIC-QVCO). IEEE Journal of Solid-State Circuits Mar. 2009; 44(3).

[16] Mazzanti A, Uggetti P, Svelto F. Analysis and design of injection-locked LC dividers for quadrature generation. IEEE Journal of Solid-State Circuits Sep. 2004; 39:1425–1432.

[17] Asyaei, Mohammad, and Emad Ebrahimi. "A low-phase noise injection-locked quadrature voltage-controlled oscillator." Analog Integrated Circuits and Signal Processing 71.2 (2012): 319-325.

[18] D. B. Leeson, “A Simple Model of Feedback Oscillator Noise Spectrum”, Proceedings of the IEEE, vol. 54, pp. 329–336, 1966.

# New codebook design algorithm for image vector quantization based on Kernel density estimation

**Ali Darroudi*, Ghazaleh Sarbisheie, Hadi Jafarnia, Jabber Parchami**

*Ali Darroudi, darroudi.a@gmail.com*

*Ghazaleh Sarbisheie, gh_sarbisheie@sadjad.ac.ir*

*Hadi Jafarnia, hadi68_jafarnia@yahoo.com*

*Jabber Parchami, jb_parchami@yahoo.com*

## Abstract

A main problem in vector quantization (VQ) is codebook designation. The traditional method used for VQ codebook generation, is the Generalized Lloyd Algorithm (GLA). The efficiency of the GLA algorithm is hardly dependent on the initial codebook selection. But, GLA algorithm usually gets trapped into local minimum of distortion, resulting in a random codebook initialization. In this paper, an effective codebook initialization algorithm based on Kernel density estimation has been proposed. Experimental results show that the proposed algorithm not only improves the quality of generated codebook but decreases the computation time compared to the GLA algorithm.

**Key words:** Vector quantization, Codebook generation, GLA algorithm, Image compression, Kernel density estimation.

## 1. Introduction

With development of electronic devices, such as mobile devices and digital cameras, digital images have been widely used. Mainly, digital images, according to their large sizes, need large storage space and high transmission rates. These constraints limit the use of digital images because mobile devices have limited memory and use wireless networks that usually have bandwidth limitations. In order to make the transmission of digital images compatible with these limitations, image compression techniques have developed and are used to convert digital images in compressed form, which decrease the storage space required and save bandwidth. This will also increase transmission speed.

Many image compression techniques have been proposed in the last two decades. These methods can be classified into two categories: lossless and lossy compression. In lossless image compression techniques, decompressed image is identical to the original image; but, lossy image compression reconstructs an approximation of the image without visual distortion from the compressed image. Clearly, lossy compression techniques can provide a higher compression rate than lossless techniques. Among lossy methods, techniques based on discrete wavelet transformation (DWT) [1], vector quantization (VQ) [2], and discrete cosine transformation (DCT) [3] are the most commonly used techniques. The above-mentioned techniques can decrease the image redundancy and as a result decrease the image size. Especially, VQ, due to its simple structure, fast decoding capability, and a high compression rate, is an efficient technique and more suitable for low power computation systems such as mobile devices.

Moreover, VQ can be applied in many applications, such as index compression [4], inverse half toning [5,6], voice conversion problem [7] and data hiding [8,9].

The VQ process can be divided into three main steps: codebook generation, encoding, and decoding. The encoding and decoding processes need a codebook. The key to VQ is a good codebook. The method most commonly used is the Generalized Lloyd Algorithm (GLA) [10]. It starts with an initial solution, which is iteratively improved using two optimality criteria until a local minimum is achieved. The performance of the GLA is hardly dependent on the selection of the initial codebook. In conventional GLA, the initial codebook is selected randomly from the training data set. Due to Non-optimal codebook initialization, it always converges to the nearest local minimum.

In the past two decades, different modifications for this method are proposed [11-18]. For example the combination of evolutionary algorithms and GLA algorithm can be noted [14-18]. Evolutionary algorithms due to their parallel search structure, reduce the possibility of convergence to the local minimum. But these algorithms need more time and more memory as the population size increases.The Pairwise Nearest Neighbor (PNN) algorithm is another alternative technique to the GLA algorithm for producing codebook. Compared to the GLA algorithm, the PNN algorithm generally has higher distortion, although it has lower computation complexity [19].

In this paper, we will present a novel algorithm to improve the quality of codebook generation. It is noted that the algorithm proposed here needs less computing time compared to the GLA algorithm; while other algorithms that improve the quality of codebook generation, such as Evolutionary algorithms combined with GLA, have very high computation time in comparison with the GLA algorithm. The remaining parts are organized as follows: Basic concepts are given in Section 2. The proposed scheme is illustrated in Section 3. Experimental results are presented in Section 4 and finally the research concludes in Section 5.

## 2. BASIC CONCEPTS

### 1-2. Vector quantization

The VQ process can be divided into three main steps: codebook generation, encoding, and decoding. In encoding procedure the image is first divided into non-overlapping p×$q$ blocks. Then each block is converted into a $k$-dimensional vector where $k=p\times q$. These vectors are called training vectors and the set of training vectors is called training set. Encoder will detect the nearest codeword for each training vector, using Euclidean distance, assumed that the codebook has been produced in past stage. The Euclidean distance between the training vector $x$ and the codeword $c_i$ can be computed using the following equation:

$$d(x,c_i) = \| x - c_i \|^2 = \sum_{j=0}^{k} (x_j - c_{ij})^2 \qquad (1)$$

In the above equation $x_j$ and $c_{ij}$ are the $j$th components of the training vector $x$ and the codeword $c_i$ respectively. After detecting the nearest codeword, the index correlated with that codeword should be saved in index table. This process is repeated for all training vectors and the achieved index table is transmitted to decoder for image reconstruction. In decoding process, the codeword related to each training vector is extracted from codebook using the index table and image is reconstructed.

### 2-2. Generalized Lloyd Algorithm

In order to produce codebook for VQ, GLA algorithm, also known as Linde–Buzo–Gary (LBG) algorithm, is usually used. The steps of this algorithm are described as follows:

1. First, $N$ vectors should be selected from the data set $X = \{ x_n \mid n = 1, 2, \ldots, M\}$ as primary codewords, randomly. The codewords are displayed with: $c_1$, $c_2$... $c_N$.

2. The closest codeword due to square of the Euclidean distance, should be discovered for each vector in the data set $X$. Then the vector is added in the related cluster by exploitation subsequent formula:

$$x_i \in Z_j, j = 1, \dots, N \iff \| x_i - c_j \| < \| x_i - c_p \|, p = 1, \dots, N \ \& \ j \neq p \qquad (3)$$

In the above equation ‖.‖ indicates Euclidean distance and $Z_j$ is $j^{th}$ cluster.

3. The new codewords will be calculated using following equation:

$$c_i^* = \frac{1}{s_i} \sum\nolimits_{x_j \in Z_i} x_j \quad, i = 1,2, \dots, N \qquad (4)$$

where $s_i$ indicates the number of vectors that belong to cluster of $Z_i$.

4. If the difference between codewords in two consecutive iterations is less than a given threshold or, a specific number of iterations has been achieved, the iteration should be stopped.

One of the most important disadvantages of GLA algorithm is that it is hardly dependent on the initial codebook. This means, if the initial codebook is not effective, the final codebook quality will be weak. Due to random codebook initialization, GLA always converges to the nearest local minimum.

## 3-2. Kernel density estimation

Kernel density estimation (KDE) is a non-parametric method to estimate the probability density function of a random variable [20]. In some fields such as signal processing and econometrics it is also named the Parzen–Rosenblatt window method. In comparison to parametric estimators where the estimator has a constant functional structure and the elements of this function are the only information we need to store, Non-parametric estimators have no constant structure and depend upon all the data points to achieve an estimate.

Let X be a random variable with an unknown density function *f(x)*. Parzen-windowing estimates the pdf of random variable X using its samples ($X_1, X_2 \dots X_N$). The kernel density estimator for X is calculated by following equation

:

$$f(x) = \frac{1}{N} \sum\nolimits_{i=1}^{N} k_h (x - X_i) = \frac{1}{Nh} \sum\nolimits_{i=1}^{N} k \left( \frac{x - X_i}{h} \right) \qquad (5)$$

where *k(.)* is the Kernel function and h is a smoothing parameter called the bandwidth.

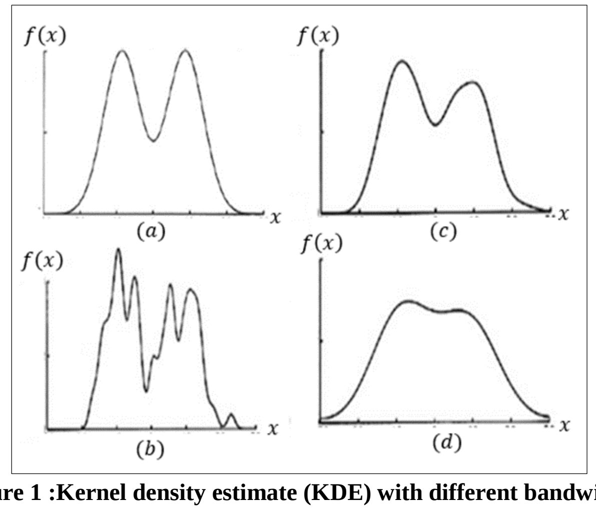


**Figure 1 :Kernel density estimate (KDE) with different bandwidths (a) True bimodal density, (b) h=0.1, (c) h=0.3, (d) h=0.6**

A kernel with subscript h is called the scaled kernel. A range of kernel functions such as uniform, triangular, normal, and others are commonly used. Due to its convenient mathematical properties, the normal (Gaussian) kernel, is often used:

$$k(x) = G(x) = \frac{1}{\sqrt{2\pi}} e^{\frac{-x^2}{2}} \qquad (6)$$

The bandwidth h controls the degree of smoothing and has a strong influence on the resulting estimate. To illustrate its effect, in figure (1), an estimation for random samples of 200 points from a bimodal density have been plotted. When h is too small the resulting curve is too wiggly and contains too many spurious data artifacts. In the other side when h is too large important features will be smoothed away.

## 3. PROPOSED METHOD

In this section a new technique for codebook initialization has been proposed. In this method, K-dimensional space is segmented into non-overlapping areas and then according to data density in each of these areas, the initial cluster centers are chosen. In order to segment the space into non-overlapping areas, we use Euclidean norm measure.

For any point in k-dimensional space, the Euclidean norm, or Euclidean length, or magnitude of a vector, measures the length of the vector. The Euclidean norm of a vector, in k-dimensional space, is calculated as follows:

$$\| x \| = \sqrt{\sum_{j=0}^{k} \left(x_j^2\right)} \qquad (7)$$

The position of a point in an Euclidean k-space is an Euclidean vector. Figure 2 shows a data set of training vectors in 2-dimensional space. In the following we refer this data set as set I.

Set I includes two different sizes Gaussian distribution clusters of 2-dimensional vectors. In this Figure, space areas are divided into L segments based on their magnitudes. As can be seen data density is not uniformly distributed in different segments. For this reason, random selection of the initial cluster centers is not the best possible choice. To have a better choice, initial cluster centers should be selected according to data density in each area. In order to obtain data distribution in different areas, distribution function of the training vectors magnitude should be estimated using Parzen windowing method with a kernel function. Figure 3 shows estimated probability density function of Euclidean lengths for training vectors of set I. By integration of the probability density function of Euclidean lengths, *f(r)*, on different areas, an estimation of data density in each area will be achieved. The number of initial cluster centers in each region should be proportional to the density of data in that region. Table 1 shows data density in each area for training vectors in set I. So, major steps of image compression for our proposed method are summarized as follows:

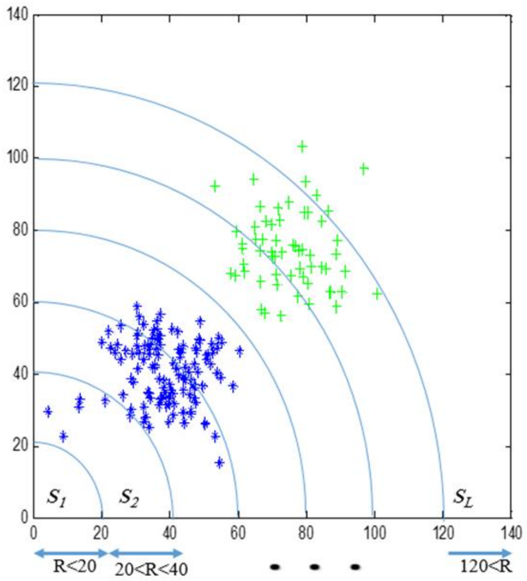


**Figure 2: Investigation of data density in different areas of 2-dimensional space for training vectors of set I. In this Figure space areas based on their magnitudes are divided into L segment.**

- Split the image into small blocks of size 4 x 4.
- Generate the training set of size N.
- Calculate the Euclidean length for all of training vectors in the training set.
- Estimate distribution function of the training vectors magnitude by Parzen windowing method
- Segment space areas based on Euclidean length

**Table 1: Data density in different areas for training vectors of set I**

| region | Data density |
|---|---|
| R<20 | 0 |
| 20<R<40 | 5% |
| 40<R<60 | 35% |
| 60<R<80 | 27% |
| 80<R<100 | 11% |
| 100<R<120 | 20% |
| 140<R | 2% |

- Integrate the pdf of Euclidean norms on different areas
- Choose initial cluster centers in each region based on data density
- Use the initial codebook generated in previous step, as input for GLA algorithm and obtain the final codebook
- Use the final codebook to obtain the index table
- Send codebook and index table to decoder.

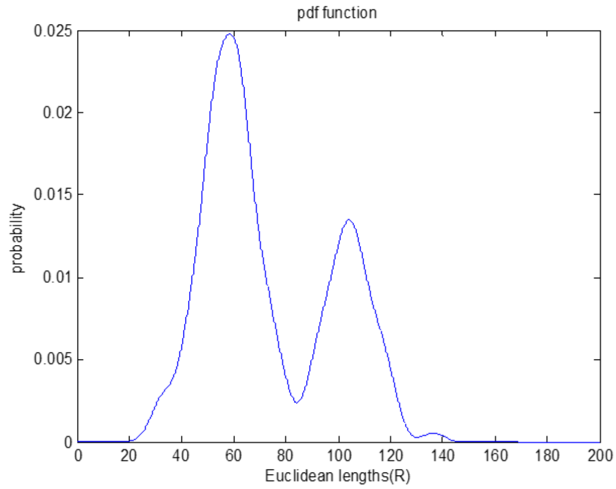


**Figure 3: Probability density function of Euclidean lengths for training vectors in set I**

## 4. Experimental results

To evaluate the performance of the proposed algorithm, four standard gray level images, has been used as our training set to generate codebooks. This set consists of four real images: Lena, boat, cameraman and airplane. The block size for these images is 4*4. Also, all computation is performed on a computer with Intel Core i5-4200M with 2.50 GHz processor and 6GB RAM. Two error metrics that are used to compare the various image compression techniques are the Mean Square Error (MSE) and the Peak Signal to Noise Ratio (PSNR). The MSE is the cumulative squared error between the compressed and the original image, whereas PSNR is a measure of the peak error.

$$MSE = \frac{1}{M.N}\sum_{y=1}^{M}\sum_{x=1}^{N}[I(x,y) - I'(x,y)]^2 \qquad (8)$$

$$PSNR = 10\log\left(\frac{255^2}{MSE}\right) \qquad (9)$$

where I(x,y) is the original image, I'(x,y) is the reconstructed image and M,N are the dimensions of the images.

**Table 2: Comparison of PSNR, RMSE and running time (second) for Lena image between three celebrated methods and proposed method**

| CB Size | GLA | | | PSO_GLA | | | Steady State MA | | | proposed | | |
|---|---|---|---|---|---|---|---|---|---|---|---|---|
| | RMSE | PSNR | Time | RMSE | PSNR | Time | RMSE | PSNR | Time | RMSE | PSNR | Time |
| 128 | 10.88 | 27.40 | 131 | 10.46 | 27.74 | 694 | 9.06 | 28.98 | 1048 | 9.47 | 28.60 | 78 |
| 256 | 9.72 | 28.38 | 211 | 9 | 29.04 | 1413 | 8 | 30.06 | 2210 | 8.24 | 29.81 | 172 |
| 512 | 8.44 | 29.60 | 417 | 7.12 | 31.10 | 2878 | 7.18 | 31 | 4163 | 7.09 | 31.11 | 280 |

Table 2 shows the comparison of PSNR, RMSE and running time for Lena image between GLA algorithm [10], PSO_GLA [16], steady-state memetic algorithm MA [18], and proposed method. Simulations show that GLA algorithm is effective but has high computation complexity. Moreover GLA algorithm usually gets trapped into local minimum of distortion, resulting in a random codebook initialization. Evolutionary algorithms combined with GLA improve the quality of generated codebook and increase the PSNR but have very high computation time. The Proposed algorithm, not only improves the quality of generated codebook but decreases the computation time compared to the GLA algorithm. In order to have a better assessment of the performance of the proposed algorithm, we also applied it on the boat, cameraman and airplane images. The results are shown in Table 3. Finally, Original Lena image of size 256×256 with 256 gray levels and reconstructed image using proposed method are shown in Fig 4.

**Table 3: Performance evaluation of proposed algorithm on different images**

| CB Size/image | Cameraman | | | boat | | | airplane | | |
|---|---|---|---|---|---|---|---|---|---|
| | RMSE | PSNR | time | RMSE | PSNR | time | RMSE | PSNR | time |
| 128 | 12.50 | 26.19 | 197 | 11.21 | 27.13 | 90 | 11.18 | 27.16 | 107 |
| 256 | 10.76 | 27.49 | 303 | 9.94 | 28.18 | 178 | 9.91 | 28.20 | 172 |
| 512 | 9.36 | 28.69 | 351 | 8.72 | 29.31 | 249 | 8.63 | 29.40 | 459 |

(a)

(b)

**Fig. 4. Original Lena image and reconstructed image using proposed method (a) original, (b) reconstructed with 512 codebook size**

## 5. CONCLUSION

An effective approach for VQ codebook generation based on density estimation has been proposed. Performance of proposed algorithm is compared with 3 celebrated methods in terms of run time and PSNR (quality of the reconstructed images). According to the experimental results, the proposed method has better performance in comparison with other algorithms.

## References

[1] C. Christopoulos, A. Skodras, T. Ebrahimi, The JPEG2000 still image coding system. An overview, IEEE Transactions on Consumer Electronics 46 (4) 1103–1127, 2000.

[2] A. Gersho, R.M. Gray, Vector Quantization and Signal Compression, Kluwer Academic Publishers, Boston, US, 1992.

[3] G.K. Wallace, the JPEG still picture compression standard, IEEE Transactions on Consumer Electronics 38 (1) xviii–xxxiv, 1992.

[4] C.H. Hsieh, J.C. Tsai, Lossless compression of VQ index with searchorder coding, IEEE Trans. Image Process. 5 (11) 1579–1582, 1996.

[5] J.Z.C. Lai, J.Y. Yen, Inverse error-diffusion using classified vector quantization, IEEE Trans. Image Process. 7 (12) 1753–1758, 1998.
[6] P.C. Chang, C.S. Yu, T.H. Lee, Hybrid LMS-MMSE inverse halftoning technique, IEEE Trans. Image Process. 10 (1) 95–103, 2001.
[7] E. Uchino, K. Yano, T. Azetsu, A self-organizing map with twin units capable of describing a nonlinear input–output relation applied to speech code vector mapping, Information Sciences 177 (21) 4634–4644, 2007.
[8] C.C. Lin, S.C. Chen, N.L. Hsueh, Adaptive embedding techniques for VQ-compressed images, Information Sciences 179 (1–2) 140–149, 2009.
[9] J.X. Wang, Z.M. Lu, A path optional lossless data hiding scheme based on VQ joint neighboring coding, Information Sciences 179 (19) 3332–3348, 2009.
[10] Y. Linde, A. Buzo, R.M. Gray, An algorithm for vector quantizer design, IEEE Trans. Commun. 28 (1) 84–95, 1980.
[11]. N.Belacel, P.hansen and N.Mladenovic, “Fuzzy J-Means: a new heuristic for fuzzy clustering”, Pattern Recognition, vol. 35, pp. 2193-2200, 2002.
[12]. R.J.Hathaway and J.C.Bezdek, “Clustering incomplete relational data using the non-Euclidean relational fuzzy c-means algorithm”, pattern Recognition Letters, vol. 23, pp. 151-160, 2002.
[13]. P.D.Pascual-Marqui, A.D.Pascual-Montano, K.Kochi and J.M.Carazo, “Smoothly distributed fuzzy c-means: a new self-organization map”, Pattern Recognition, vol. 34, pp. 2395-2402, 2001.
[14]. U.Maulik and M.Pakhira, "Clustering using simulated annealing with probabilistic redistribution", International Journal of Pattern Recognition and Artificial Intelligence, vol. 15, no. 2, pp. 269 285, 2001
[15].U.Maulik and S.Bandyopadhyay, "Genetic algorithm based clustering technique", Pattern Recognition, vol. 33, pp. 1455-1465, 2000
[16]Merwe, D.W.: Engelbrecht A P. Data Clustering Using Particle Swarm Optimization. Evolutionary Computation. CEC '03. The 2003 Congress on. 215 – 220, 2003.
[17] Q. Chen, J. Yang, J. Gou, Image compression method using improved PSO vector quantization. Lecture Notes in Computer Science, pp. 490-495, 2005.
[18] C.M. Ou, Vector quantization based on steady-state memetic algorithm. *Journal of Marine Science and Technology*, pp. 553-557, 2010.
[19] W.H. Equitz, A new vector quantization clustering algorithm, IEEE Trans. Acoust. Speech Signal Process. 37 (10) 1568–1575, 1989
[20] B.W.Silverman, *Density Estimation for Statistics and Data Analysis*, Chapman and Hall, London, 1986.

# Application of response surface methodology for optimization of cadmium (II) in aqueous solution by chitosan/MCM-41

**Abbas Teimouri* , Fatemeh Dadkhah Tehrani**
*1. Chemistry Department, Payame Noor University, 19395-3697, Tehran, Islamic Republic of Iran. E-mail: a_teimouri@pnu.ac.ir; a_teimoory@yahoo.com; Fax: +98-31-33521802; Tel: +98-31-33521804*

**Abstract**
In this study, removal of cadmium from aqueous solution was conducted by chitosan and MCM-41 nano composite. Response surface methodology (RSM) was used for modeling and optimizing the process, and to gain a better understanding of the process performance. Centered Composite Design (CCD) was used as the experimental design .Parameters effects such as temperature, pH, contact time, initial Cd(II) concentration and adsorbent dose on the adsorption process were studied. The numerical optimization revealed that the optimum removal (87.15%) obtained at ct/mcm-41 dosage of 0.1g, initial Cd (II) concentration of 20 $mgL^{-1}$, contact time of 30 min, temperature $30^0$c and pH of 6.

**Key words:** Aqueous solution, Cd (II) removal, Response surface methodology

## 1. Introduction

Heavy metals represent a group of dangerous environmental pollutants that due to their toxic effects on human health in concentrations above the permissible limits cause widespread concerns [1]. Cadmium (II), as an example of toxic metals, is of significant environmental concern due to high mobility [2].

According to the guidelines of the World Health Organization, the allowable limit of cadmium in water is 0.003 mg/L. This stringent limit of cadmium in potable water is due to cadmium's severe toxicity and effect on the health of humans, animals and plants. Moreover, cadmium has been found to accumulate primarily in the kidneys and has a relatively long biological half-life of 10 to 35 years in humans. It is believed that the kidneys are the target organs for cadmium toxicity [3].

A potential source of cadmium contamination in drinking water is industrial wastewater. Industrial sources include the waste from the manufacturing processes of smelting, pesticides, fertilizers, dyes, pigments, refining, textile operations, etc [4].

Several technologies, such as electro coagulation process, ion exchange, emulsion liquid membrane, reverse osmosis processes and adsorption have been tested for heavy metal removal from the industrial wastewater to decrease their impact on the environment. Nevertheless, the adsorption seems to be the most suitable method for the removal of metals in the case of low concentration due to low cost and high efficiency.Many adsorbents such as activated carbon, clays, metal oxides, silica , zeolite and chitosan have been used for the metals removal [5-7].

Chitosan (CS) is a cationic biopolymer obtained from deacetylation of chitin which is the second most abundant biopolymer in nature [8,9]. Chitosan has received considerable attention as an excellent natural adsorbent to remove many pollutants including fluoride, dyes, heavy metal ions and HA due to the presence of amino and hydroxyl groups, which can serve as the active sites [8–12].

It is necessary for adsorbents and photo catalysts to have many ion exchange sites and high surface area. The synthesis of mesoporous materials offers the possibility of preparing catalysts that are applicable in many industrial processes. The characteristics

of high surface area, large adsorption capacity and porous structure make them great promising candidates in oil refining, petro chemistry, organic synthesis and waste treatment [13,14].In particular, the mesoporous silicate MCM-41 has the potential to be used as an adsorbent or support for catalyst due to its hexagonal arrangement of pores with typical diameter of 1.5–10 nm, high surface area, large pore volume, and high thermal stability [15–19].

In this work, for the first time, we synthesized the Chitosan/ MCM-41 nano composite adsorbent for Cd (II) removal. We report the preparation, characterization and Cd (II) adsorption ability of Chitosan / MCM-41 as well as the related adsorption isotherms and kinetics. Also, the effects of different experimental conditions, such as initial Cd(II) concentration, the initial pH value of the cadmium solution, adsorbent dose, contact time and adsorption temperature, were investigated.

## 2. Materials and methods

### 2.1. Materials

Chitosan was purchased from Sigma-Aldrich. Analytical grade hexadecyltrimethylammonium bromide (CTAB), acetic acid, hydrochloric acid (37%), sodium hydroxide (NaOH) were all purchased from Aldrich and used without further purification. Deionized distilled water was used in the preparation of all solutions.

### 2.2. Synthesis of MCM-41 mesoporous silica

MCM-41 was synthesized using CTAB as the structure directing reagent, the TEOS as a silica precursor, distilled water, and $NH_3$ as a base source at ambient temperature [20]. MCM-41 was prepared in base condition under room temperature as follows: 2.4 g CTAB surfactant were mixed with 120 mL distilled water and then 10 mL of $NH_3$ was added into the solution with stirring and heating. When the solution became homogeneous, 10 mL TEOS was added into the homogeneous solution, and the solution was stirred for 24 h. After aging for 48 h, the solid product was filtered with distilled water, dried in an oven at 70 $^0$C, and followed by calcination in air at 550 $^0$C for 6 h.

### 2.3. Preparation of Chitosan/ MCM-41 nano composite

0.25 g of MCM-41 was immersed in 5 mL of distilled water to make slurry. 0.02 g of chitosan was dissolved in (2%, v/v) acetic acid aqueous solution and stirred for 1 h. This solution was added to the slurry and the mixture was stirred for 30 min. 5% of glutaraldehyde aqueous solution at a 40:1 volume ratio of chitosan solution was added and stirred vigorously for 5 min. The mixture was stirred for 2 h and soaked in an ultrasonic bath for 30 min. The wet bead mixture was transferred to a refrigerator at 4 ◦C for 24 h to undergo complete cross-linking reaction and washed to neutral pH and dried in oven at 50 ◦C.

### 2.4. Characterizations

The samples were evaluated by X-ray diffraction (XRD) using a Philips X'PERT MPD X-ray diffractometer (XRD) with Cu Kα (1.5405 Aº). Data sets were arranged over the range of 0º– 90º, with a step size of 0.02º, and a count rate of 3.0º/min. The morphology of the samples was evaluated using a SEM (JSM-6300, Tokyo, Japan) IR spectra were recorded on JASCO FT/IR-680 PLUS spectrometer. The BET specific surface areas and BJH pore size distribution of the nano composites were evaluated using a Series BEL SORP 18.

**2.5. Batch experiments**

A series of batch experiments were conducted to determine the Cd (II) removal using different condition of experiments including pH, contact time, initial Cd(II) concentration, adsorbent dose and temperature. Experiments were performed in the beaker containing 10 mL Cd (II) solutions (5- 25 mgL$^{-1}$.) with the desired pH(3-7) which were set by 0.1 M NaOH and 0.1 M HCl solutions and the dosage of adsorbent prepared application (0.025-1.25g). beakers were shaken vigorously for (20-60) min at temperature of (25-45$^0$c). Upon centrifuging at 5000 rpm, supernatants were filtered. The concentration of residual Cd (II) in the filtered solution was determined via atomic absorption spectrometry The Cd (II) removal efficiency (RE %) was calculated by the following equation:

$$R\,\% = (C0 - Ce)/\,C0 \qquad (1)$$

The mass q of Cd (II) adsorbed at equilibrium per gram of membrane (mg/g) was quantified as follows:

$$qe \;=\; (C0 - Ce)\; v\;/m \qquad (2)$$

where c0 and ce are the initial and equilibrium concentrations of Cd(II) ions in the solution (mg/L), respectively, V is the volume of solution (L) and m is the mass of dry membrane (g).

**2.6. Experimental design and optimization**

Response surface methodology has 4 major steps, which are experimental design, model fitting, model validation and condition optimization. Experimental designs such as Central Composite Designs (CCD) are useful for RSM because they do not require an excessive number of experimental runs.

The central composite design (CCD) under RSM was used for determining the optimum conditions of Cd (II) removal from aqueous solution by varying the five independent factors of initial Cd (II) concentration, pH, contact time, temperature and dosage of chitosan/MCM-41. The CCD is an effective design which is capable of covering the combination of variables simultaneously, and could be applied to the modeling and analysis of multiple parameters. In this design, the number of experiments (N) is calculated by the following equation:

$$N = 2^k + 2k + n_c \qquad (3)$$

where k is the number of variables and $n_c$ is the number of central points. The series of applied experiments in CCD are: (1) factorial points, (2) axial or star points, and (3) central points.

The coded levels and the natural values of these factors set in the chosen variables were solution pH ($x_1$), initial concentration of Cd (II) (mg L$^{-1}$)($x_2$), chitosan/MCM-41 dosage (g L$^{-1}$)($x_3$) , contact time(min)($x_4$) and temperature($x_5$) . For statistical calculations, the variables were coded as x according to the following equation [21]:

$$x_i = \frac{Xi - Xo}{\Delta Xi} \qquad (4)$$

where $X_0$ is the value of $X_i$ at the central point, and $\Delta X$ is the step change.

The percentage of Cd (II) removal efficiency as the response (Y) of the experiments and the behavior of the system was explained by the following quadratic equation:

$$Y = \beta o + \sum \beta iXi + \sum \beta iiXi^2 + \sum \beta\, ijXiXj + \varepsilon \quad (5)$$

where Y is the response, $ß_0$, ßi , ßii are the regression coefficients of variables for intercept, linear, quadratic and interaction terms, respectively, $X_i$ and $X_j$ are the independent variables and ε is the residual term.

## 3. Results and discussions

### 3.1. FT-IR analysis

FT-IR spectra of Chitosan, MCM-41, and Chitosan / MCM-41 nanocomposites are shown in Fig. 1. In the spectrum of Chitosan, as shown in Fig. 1a, the band at 3448.1 $cm^{-1}$ and 2361.41 cm-1 was attributed to the stretching vibrations of the Chitosan structure framework.

In the spectrum of MCM-41, as shown in Fig. 1b, a broad and strong band at 3442.31$cm^{-1}$, which could be attributed to the O–H stretching bonds of silanol groups. The vibrations of Si–O–Si could be seen at 1096.33 $cm^{-1}$ (asymmetric stretching) and 968.09 $cm^{-1}$ (symmetric stretching).

In Fig. 2, the FT-IR spectrum of Chitosan, MCM-41 nano composite before and after adsorption Cd (II) - was provided. The band at below of the 500 $cm^{-1}$ is related to Cd (II) adsorption.

### 3.2. XRD analysis

X-ray diffraction (XRD) patterns of the adsorbents were evaluated using Cu Kα radiation (λ=1.5405 A°).

In the XRD of Chitosan, MCM-41, the sharp lines at 10 and 20 and 22.5° were shown in Fig 3.

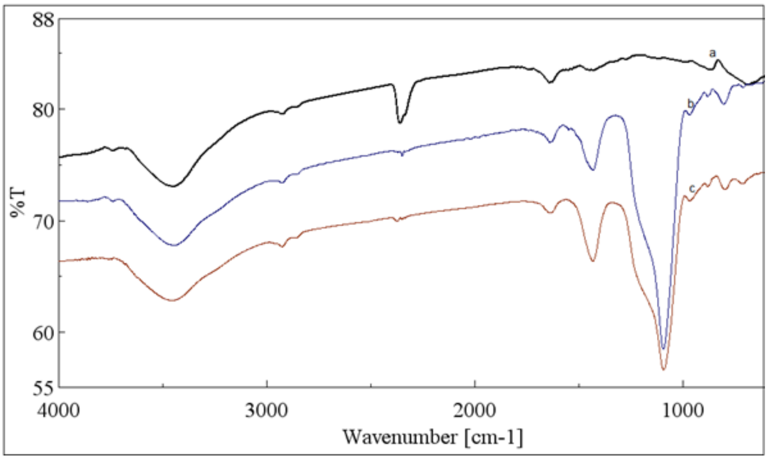


**Fig. 1. FTIR spectra of a) Chitosan; b) MCM-41 and c) Chitosan, MCM-41 nanocomposites.**

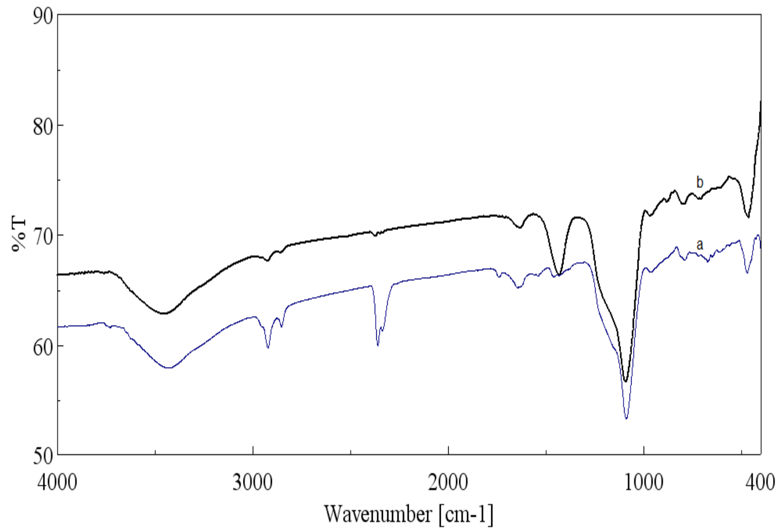


**Fig.2. FTIR spectra of a) Chitosan, MCM-41 nano composite before adsorption and b) after Cd (II) adsorption.**

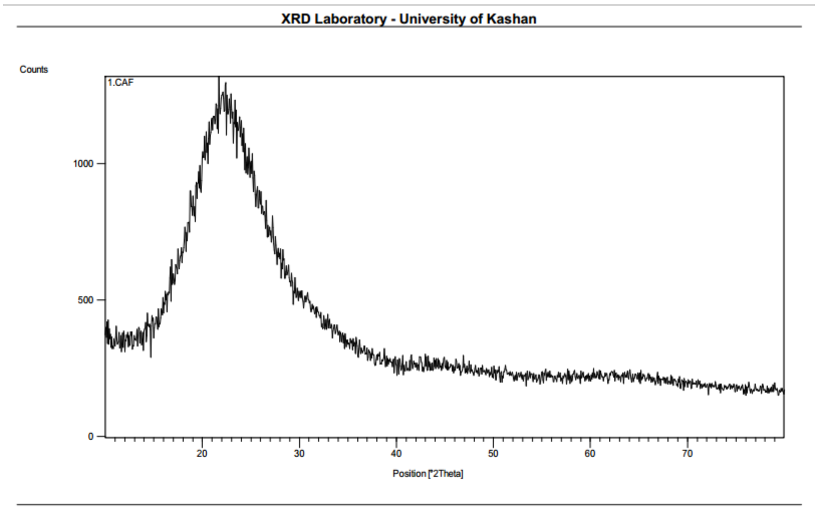


**Fig.3. XRD patterns of Chitosan, MCM-41 nano composites**

## 4. Conclusions

In this research, a novel low-cost bio sorbent, Chitosan/ MCM-41 nano composite material, was prepared using environmentally friendly material such as Chitosan and MCM-41. Application of Chitosan/ MCM-41 could be as an effective adsorbent for removing the Cd (II) from contaminated water resources. This study tried to synthesize and characterize Chitosan/ MCM-41 and then examine their performance on Cd (II) removal from aqueous solution using CCD under the RSM. The potential of synthesized Chitosan/ MCM-41 to remove Cd (II) from aqueous solutions was investigated in batch experiments, where several parameters such as the contact time, initial Cd (II) concentration, pH, temperature and Chitosan/ MCM-41 dosage were investigated. The obtained results demonstrated that Chitosan/ MCM-41 can promisingly be used as an efficient sorbent for Cd (II). The optimum removal efficiency of Cd (II) achieved by setting the experiment with Chitosan/ MCM-41 dosage at 0.1 g $L^{-1}$, contact time at 30 min, initial Cd (II) concentration at 20 $mgL^{-1}$, pH at 6 and temperature at 30 $^{o}C$. Results also prove that the RSM is a powerful tool for optimizing and the operational conditions of Cd (II) removal efficiency using Chitosan/ MCM-41.

## References

[1] S M Al-Garni, S A. Biosorption of lead by Gram-ve capsulated and non-capsulated bacteria. Water; 31 (3): 345-350,2005.

[2] M P Waalkes, J Inorg. Cadmium carcinogenesis in review. Biochem; 79 (1-4): 241-244,2000.

[3] Y H Li, S Wang, Z Luan, J Ding, C Xu, D Wu. Adsorption of cadmium(II) from aqueous solution by surface oxidized carbon nanotubes.Carbon; 41 (5): 1057–1062,2003.

[4] K S Rao, M Mohapatra, S Anand, P Venkateswarlo. Review on cadmium removal from aqueous solutions. Int.J. Eng. Sci. Technol; 2 (7):81–103,2010.

[5] Y C Sharma. Thermodynamics of removal of cadmium by adsorption on an indigenous clay. Chem. Eng. J; 145 (1) 64-68,2008.

[6] H K Boparai, M Joseph, D M O'Carroll. Kinetics and thermodynamics of cadmium ion removal by adsorption on to nano zerovalent iron particles. J. Hazard. Mater; 186 (1) 458-465,2011.

[7] G Q Tan, D Xiao. Adsorption of cadmium ion from aqueous solution by ground wheat stems J. Hazard. Mater; 164 (2-3) 1359-1363,2009.

[8] W S Wan Ngah, L C Teong, M A.K M Hanafiah,.Adsorption of dyes and heavy metal ions by chitosan composites: a review. Carbohyd. Polym;83 (4) :1446–1456,2011.

[9] P Miretzky, A F Cirelli. Fluoride removal from water by chitosan derivatives and composites: a review. J. Fluorine Chem; 132 (4): 231–240,2011.

[10] W S. Wan Ngah, S Fatinathan, N A Yosop.Isotherm and kinetic studies on the adsorption of humic acid onto chitosan-$H_2SO_4$ beads. Desalination; 272 (1-3):293–300,2011.

[11] L Zhao, F Luo, J M Wasikiewicz, H Mitomo, N Nagasawa, T Yagi, M Tamada,F Yoshii. Adsorption of humic acid from aqueous solution onto irradiationcrosslinked Carboxymethylchitosan. Bioresour. Technol; 99 (6): 1911–1917,2008.

[12] W S Wan Ngah, M K M Hanafiah, S S Yong. Adsorption of humic acid from aqueous solutions on crosslinked chitosan-epichlorohydrin beads: kinetics and isotherm studies. Colloid Surf. B; 65 (1): 18–24,2008.

[13] A Corma,.From microporous to mesoporous molecular sieve materials and their use in catalysis. Chem. Rev. 97 (6) 2373–2420,1997.

[14] A De Stefanis, S Kaciulis, L Pandolfi. Preparation and characterizationof Fe–MCM-41 catalysts employed in the degradation of plasticmaterials, Micropor. Mesopor. Mater; 99 (1-2): 140–148,2007.

[15] R Anwander, I Nagl, M Widenmeyer, G Engelhardt, O Groeger,C Palm, T Röser. Surface characterization and derivatization of MCM41 silicas via silazane silylation.J. Phys. Chem. B 104 (15): 3532–3544,2000.

[16] C T Kresge, M E Leonowicz, W J Roth, J C Vartuli, J S Beck. Ordered mesoporous molecular sieves synthesized by a liquid-crystal template mechanism.. Nature ;359 : 710–712,1992.

[17] J S Beck, J C Vartuli, W J Roth, M E Leonowicz, C T Kresge, K D Schmitt, C TW Chu, D H Olson, E W Sheppard, S B McCulle, J B Higgins, J L Schlender. J Am. Chem. Soc; 144 (27) :10834–10843,1992.

[18] J. Choma, M. Jaroniec, W. Burakiewicz-Mortka, M. Kloske. Critical appraisal of classical methods for determination of mesopore size distributions of MCM-41 materials. Appl. Surf. Sci; 196 (1-4) :216–223,2002.

[19] G.K. Chuah, X. Hu, P. Zhan, S. Jaenicke. Catalysts from MCM-41: framework modification, pore size engineering, and organic–inorganichybrid materials. J. Mol. Catal. A; 181 (1-2): 25–31,2002.

[20] Q. Cai, W.Y. Lin, F.S. Xiao, W.Q. Pang, X.H. Chen, B.S. Zou. The preparation of highly ordered MCM-41 with extremely low surfactant concentration. Microporous Mesoporous Mater ;32 (1-2): 1-15,1999.

[21] A.R. Khataee Optimization of UV-promoted peroxydisulphate oxidation of C.I. Basic Blue 3 using response surface methodology. Environ. Technol. 31 (1) :73-86,2010.

پژوهش های نوین
علوم مهندسی

۰۲۱ ۴۳ ۸۵ ۷۱ ۲۴
۰۲۶ ۳۲ ۷۴ ۷۱ ۵۸
۰۲۱ ۳۳ ۲۰ ۲۴ ۸۷
۰۲۶ ۳۲ ۷۲ ۴۷ ۸۷
تهران: افسریه،۱۵متری چهارم،کوچه ۳۸، پلاک ۲۸ ، واحد ۲
کرج: چهارراه هفت‌تیر،خیابان لاله ۱ ،پلاک ۱۴ ،طبقه همکف